

LOW REYNOLDS NUMBER AERODYNAMICS OF FLAPPING AIRFOILS IN
HOVER AND FORWARD FLIGHT

A THESIS SUBMITTED TO
THE GRADUATE SCHOOL OF NATURAL AND APPLIED SCIENCES
OF
MIDDLE EAST TECHNICAL UNIVERSITY

BY

ERKAN GÜNAYDINOĞLU

IN PARTIAL FULFILLMENT OF THE REQUIREMENTS
FOR
THE DEGREE OF MASTER OF SCIENCE
IN
AEROSPACE ENGINEERING

SEPTEMBER 2010

Approval of the thesis:

**LOW REYNOLDS NUMBER AERODYNAMICS OF FLAPPING AIRFOILS
IN HOVER AND FORWARD FLIGHT**

submitted by **ERKAN GÜNAYDINOĞLU** in partial fulfillment of the requirements
for the degree of **Master of Science in Aerospace Engineering Department,**
Middle East Technical University by,

Prof. Dr. Canan Özgen
Dean, Graduate School of **Natural and Applied Sciences**

Prof. Dr. Ozan Tekinalp
Head of Department, **Aerospace Engineering**

Assoc. Prof. Dr. D. Funda Kurtuluş
Supervisor, **Aerospace Engineering Dept., METU**

Examining Committee Members:

Prof. Dr. İsmail H. Tuncer
Aerospace Engineering Dept., METU

Assoc. Prof. Dr. D. Funda Kurtuluş
Aerospace Engineering Dept., METU

Prof. Dr. Yusuf Özyörük
Aerospace Engineering Dept., METU

Asst. Prof. Dr. Oğuz Uzol
Aerospace Engineering Dept., METU

Dr. Mustafa Kaya
The Scientific & Technological Council of Turkey
(TUBİTAK-SAGE)

Date:

13 / 9 / 2010

I hereby declare that all information in this document has been obtained and presented in accordance with academic rules and ethical conduct. I also declare that, as required by these rules and conduct, I have fully cited and referenced all material and results that are not original to this work.

Name, Last Name : Erkan Günaydinođlu

Signature :

ABSTRACT

LOW REYNOLDS NUMBER AERODYNAMICS OF FLAPPING AIRFOILS IN HOVER AND FORWARD FLIGHT

Günaydinođlu, Erkan

M.Sc., Department of Aerospace Engineering

Supervisor : Assoc. Prof. Dr. D. Funda Kurtuluş

September 2010 , 73 pages

The scope of the thesis is to numerically investigate the aerodynamics of flapping airfoils in hover and forward flight. The flowfields around flapping airfoils are computed by solving the governing equations on moving and/or deforming grids. The effects of Reynolds number, reduced frequency and airfoil geometry on unsteady aerodynamics of flapping airfoils undergoing pure plunge and combined pitch-plunge motions in forward flight are investigated. It is observed that dynamic stall of the airfoil is the main mechanism of lift augmentation for both motions at all Reynolds numbers ranging from 10000 to 60000. However, the strength and duration of the leading edge vortex vary with airfoil geometry and reduced frequency. It is also observed that more favorable force characteristics are achieved at higher reduced frequencies and low plunging amplitudes while keeping the Strouhal number constant. The computed flowfields are compared with the wide range of experimental studies and high fidelity simulations thus it is concluded that the present approach is applicable for investigating the flapping wing aerodynamics in

forward flight. The effects of vertical translation amplitude and Reynolds number on flapping airfoils in hover are also studied. As the vertical translation amplitude increases, the vortices become stronger and the formation of leading edge vortex is pushed towards the midstroke of the motion. The instantaneous aerodynamic forces for a given figure-of-eight motion do not alter significantly for Reynolds numbers ranging from 500 to 5500.

Keywords: Unsteady Aerodynamics, Micro Aerial Vehicles, Flapping Airfoils

ÖZ

HAVADA ASILI KONUMDA VE İLERİ UÇUŞTA ÇIRPAN KANAT KESİTLERİNİN DÜŞÜK REYNOLDS SAYILI AERODİNAMİĞİ

Günaydinoğlu, Erkan

Yüksek Lisans, Havacılık ve Uzay Mühendisliği Bölümü

Tez Yöneticisi : Doç. Dr. D. Funda Kurtuluş

Eylül 2010, 73 Sayfa

Bu tezin amacı havada asılı konumda ve ileri uçuşta çırpan kanat kesitlerinin aerodinamiğini sayısal olarak incelemektir. Kanat kesitleri etrafındaki akış alanları korunum denklemlerinin hareketli ve/veya bozulan çözüm ağları üzerinde çözümü kullanılarak hesaplanmıştır. Reynolds sayısının, indirgenmiş frekansın ve kanat kesiti geometrisinin ileri uçuşta daimi olmayan çırpan kanat aerodinamiğine etkisi sade-dalma ve dalma-yunuslama hareketi için incelenmiştir. 60000 ile 10000 arasındaki Reynolds sayılarında her iki hareket boyunca kaldırma kuvveti artışına neden olan esas mekanizmanın dinamik taşıma kaybı olduğu görülmüştür. Bunun ile birlikte hücum kenarı girdabının gücü ve kanat üzerinde kalma süresi kanat kesiti geometrisi ve indirgenmiş frekans ile değişmektedir. Ayrıca yüksek indirgenmiş frekans ve düşük dalma genliklerinde, Strouhal sayısı sabit tutulurken, daha uygun kuvvet özellikleri elde edildiği görülmüştür. Hesaplanan akış alanları geniş çaplı deneysel çalışmalarla ve yüksek kesinlikli benzetimlerle karşılaştırılmış ve mevcut yöntemin ileri uçuşta çırpan kanat aerodinamiğini araştırmak için uygulanabilir olduğu

gösterilmiştir. Havada asılı konumdaki kanat kesiti aerodinamiğine Reynolds sayısının ve düşey öteleme genliğinin etkileri de incelenmiştir. Düşey öteleme genliği artarken, girdapların daha güçlü olduğu ve hücum kenarı girdabının oluşumunun hareketin ortalarına doğru ilerlediği görülmüştür. Sekiz şeklinde hareket eden kanat kesitlerinin anlık kuvvetlerinin 500 ile 5500 Reynolds sayıları arasında önemli bir ölçüde değişmediği gözlemlenmiştir.

Anahtar Kelimeler: Zamana Bağlı Aerodinamik, Mikro Hava Araçları, Çırpan Kanat Kesitleri

To my parents

ACKNOWLEDGMENTS

I would like to express my deep and sincere gratitude to my supervisor Assoc. Dr. D. Funda Kurtuluş, whose kindness, patience, academic experience and knowledge is invaluable for me at all steps of this thesis study. Without her enthusiasm, energy and support, I could not be able to complete this study

I would like to thank my jury members Prof. Dr. İsmail H. Tuncer, Prof. Dr. Yusuf Özyörük, Asst. Prof. Dr. Oğuz Uzol and Dr. Mustafa Kaya for reviewing my thesis.

I would like to thank Mert, Engin, Sezgi, Efe, Bayram, Yashar, Hasan, Seyfullah, Eser and Sedat for being with me on the boot camps of Aerospace Engineering Department where we spent half of our lives.

Lastly, but most importantly, I would like to express my eternal gratitude to my parents for their love, support and encouragement throughout my life.

This study was supported by 105M230 TUBITAK project.

TABLE OF CONTENTS

ABSTRACT.....	iv
ÖZ.....	vi
ACKNOWLEDGMENTS	ix
TABLE OF CONTENTS.....	x
LIST OF TABLES	xii
LIST OF FIGURES	xiii
CHAPTERS	
1. INTRODUCTION.....	1
2. LITERATURE SURVEY	3
2.1 Forward Flapping Flight Studies.....	4
2.2 Hovering Studies.....	6
3. NUMERICAL METHOD.....	11
3.1 Governing Equations.....	11
3.2 Computational Grid and Boundary Conditions	13
3.3 Grid and Time-step Refinement Study	16
3.4 Forward Flight Kinematics	17
3.5 Hovering Kinematics	18
3.6 Significant Non-dimensional Parameters.....	19
4. FORWARD FLIGHT RESULTS	21

4.1	Baseline Motion and Related Parameters	21
4.2	Pure Plunge Case.....	24
4.3	Combined Pitch-Plunge Case.....	29
4.4	Effect of Airfoil Geometry.....	32
4.5	Effect of Reduced Frequency.....	37
4.6	Effect of Reynolds Number	41
5.	HOVERING RESULTS	45
5.1	Hovering Kinematics	45
5.2	Effect of Vertical Translation.....	46
5.3	Effect of Reynolds Number	58
6.	CONCLUDING REMARKS	63
	REFERENCES.....	67

LIST OF TABLES

TABLES

Table 4.1 All investigated cases for forward flight of SD7003 and flat plate	24
Table 5.1 Mean lift and drag coefficients for different Y values at Re=1000	56
Table 5.2 Efficiencies and lift-to-drag ratios for different Y values at Re=1000	57

LIST OF FIGURES

FIGURES

Figure 2.1 Effective angle of attack generation by flapping motion in a steady current [14]	4
Figure 3.1 Unstructured grid around SD7003, in open bounded domain (left) and its distribution near airfoil (right)	14
Figure 3.2 Unstructured grid around flat-plate, in open bounded domain (left) and its distribution near the flat plate (right)	15
Figure 3.3 Structured grid around SD7003 airfoil, in open bounded domain (left) and its distribution near airfoil (right)	15
Figure 3.4 Time histories of lift and drag coefficients with different grids (top) and with different time-steps (bottom) in hover for three periods of flight	16
Figure 3.5 Time histories of lift coefficient history with different grids around SD7003 (left) and flat plate (right)	17
Figure 4.1 Time histories of geometric and effective angle of attack over one period of pure plunging and combined pitching plunging at $Re=60000$ and $k=0.25$..	23
Figure 4.2 Normalized u-velocity contours from present computation (left column), PIV experiment of AFRL (middle column) and URANS solution of Michigan University (right column) for pure plunge, $Re=60,000$ $k=0.25$ [22]	26
Figure 4.3 Normalized out-of-plane component of vorticity contours from present computation (left column), PIV experiment of AFRL (middle column) and URANS solution of Michigan Uni. (right column) for pure plunge, $Re=60,000$, $k=0.25$ [22]	27
Figure 4.4 Lift coefficient history (left) and drag coefficient history (right) for pure plunge motion at $Re=60,000$ and $k=0.25$. The results of thesis work are reported as METU results in Ref. [22]	28
Figure 4.5 Normalized u-velocity contours from present computation (left), PIV experiment of TU Braunschweig (middle) and PIV experiments of AFRL (right) for combined pitch-plunge, $Re=60,000$ $k=0.25$ [22]	29

Figure 4.6 Normalized out-of-plane component of vorticity contours from present computation (left column), PIV experiment of TU Braunschweig [22] (middle column) and PIV experiments of AFRL [22] (right column) for combined pitch-plunge, $Re=60,000$ $k=0.25$	30
Figure 4.7 Lift coefficient history (left) and drag coefficient history (right) for combined pitch-plunge motion at $Re= 60,000$ and $k=0.25$. The results of thesis work are reported as METU results in Ref. [22]	31
Figure 4.8 Normalized out-of-plane component of vorticity contours from present computation (left column), PIV experiment of University of Michigan [22] (middle column) and PIV experiment of AFRL [22] (right column) for combined pitch-plunge, $Re=60,000$ $k=0.25$	33
Figure 4.9 Normalized out-of-plane component of vorticity contours from present computation (left column), URANS computations of Uni. of Michigan [22] (middle column) and PIV experiments of Uni. Of Michigan [22] (right column) for combined pitch-plunge, $Re=60,000$ at $k=0.25$	35
Figure 4.10 Lift coefficient history (left) and drag coefficient history (right) for pure plunge motion of a flat plate at $Re= 60,000$ and $k=0.25$ [22]	36
Figure 4.11 Lift coefficient history (left) and drag coefficient history (right) for combined pitch-plunge motion of a flat plate at $Re= 60,000$ and $k=0.25$ [22]	36
Figure 4.12 Time histories of geometric and effective angle of attack over one period of pure plunging and combined pitching plunging at $Re=60000$ and $k=0.25$..	37
Figure 4.13 Contours of normalized u-velocity for pure-plunge from computation (left column) and experimental results from [61] (right column) at $Re=60000$, $k=3.93$ and $h_0=0.05$	38
Figure 4.14 Contours of normalized vorticity from present computation (left column), experimental results from [61] (right column) at $Re=60000$, $k=3.93$ and $h_0=0.05$	39
Figure 4.15 Normalized vorticity contours for combined pitch-plunge, at $Re=60000$, $k=3.93$ and $h_0=0.05$	40
Figure 4.16 Time histories of lift coefficients (left) and drag coefficients (right) for high frequency cases, at $Re=60000$, $k=3.93$ and $h_0=0.05$	41
Figure 4.17 Time histories of lift coefficients for pitch-plunge (left) and pure plunge (right) at three different Reynolds numbers.....	42

Figure 4.18 Time histories of drag coefficients for pitch-plunge (left) and pure plunge (right) at three different Reynolds numbers.....	42
Figure 4.19 Contours of normalized vorticity for combined pitch-plunge motion at Re=10,000 (left column), Re=30,000 (middle column) and Re= 60,000 (right column), k=0.25.....	43
Figure 5.1 Sample figure-of-eight motion for Y=0.5. Positions of airfoils each with 0.05T time interval.....	46
Figure 5.2 Flapping paths of hovering airfoil with different vertical translation amplitudes.....	46
Figure 5.3 Normalized vorticity contours of Y=0 hovering at Re=1000. Red regions denote positive vorticity (CCW swirling) and blue regions denote negative vorticity (CW swirling)	48
Figure 5.4 Normalized vorticity contours of Y=0.5 hovering at Re=1000. Red regions denote positive vorticity (CCW swirling) and blue regions denote negative vorticity (CW swirling)	49
Figure 5.5 Normalized vorticity contours of Y=1 hovering at Re=1000. Red regions denote positive vorticity (CCW swirling) and blue regions denote negative vorticity (CW swirling)	50
Figure 5.6 Time histories of lift coefficients for hovering motions with different vertical translation amplitudes at Re=1000	52
Figure 5.7 Time histories of drag coefficients for hovering motions with different vertical translation amplitudes at Re=1000	53
Figure 5.8 Pressure coefficient contours with streamlines for three different Y values at t/T=0.4, Re=1000.....	54
Figure 5.9 Efficiencies and mean lift coefficients for investigated hovering motions	57
Figure 5.10 Time histories of lift and drag coefficients for Y=0.5 hovering at different Reynolds numbers.....	58
Figure 5.11 Instantaneous normalized vorticity contours for at the beginning of the period for different Reynolds numbers.....	60
Figure 5.12 Mean lift (left) and drag (right) coefficients for Y=0.5 hovering at different Reynolds numbers.....	61

CHAPTER I

INTRODUCTION

The physics of animal flight is one of the main research topics for biologists in which flapping flight shows itself as a favorable design after 350 million years of natural selection [1]. The animal flight fascinates humans for centuries with its beauty but there are much more impressive facts in terms of their flight performance. For instance a supersonic aircraft as SR-71 that is cruising at Mach 3 covers 32 body lengths per second whereas a European starling can cover 120 body lengths per second. A Barn Swallow has a roll rate of $5000^\circ/\text{s}$ where as the typical value for an aerobatic aircraft is $720^\circ/\text{s}$ [2]. It is also important to note that if a typical conventional aircraft would fly at the same Reynolds number with the insects; the air must be as viscous as honey.

The recent advances in micro-technologies led the engineers to miniaturize the air vehicles as small as possible. To achieve this, Defense Advanced Research Projects Agency defined the concept of micro aerial vehicles (MAV) in 1997. A MAV is defined to be an aircraft with maximum dimensions of 15 cm and maximum weight of 90 grams [3]. The primary objectives of MAVs are surveillance, detection, communications and the placement of unattended sensors. The MAVs have advantages as rapid deployment, real time data acquisition, low radar area and low noise [4].

The flapping wing MAV seems to be the best configuration than its counterparts. Fixed-wing configurations do not have hover capability which will be an important

disadvantage to fly in a confined space. On the other hand the rotary wings cannot operate near walls where the performance and stability of the vehicle is strongly affected by existence of solid boundaries.

Birds and insects fly at different Reynolds numbers, thus use different mechanisms to fly. Insects fly at laminar regime and generate highly vortical flowfields. In hover, the insects can flap their wing in horizontal direction with great changes in pitch angle. Thus they can create lift without forward velocity [5]. On the other hand, birds flap their wings in vertical direction and they need to have free stream to create lift. Thus they cannot hover and operate at higher Reynolds numbers generally in transitional regime. This thesis includes the numerical study of bird-like and insect-like flight.

The present thesis consists of six chapters. Second chapter includes the review of literature in terms of the experimental, numerical and analytical studies on flapping flight. In third chapter the numerical methods used in this study are explained in details. The fourth chapter is devoted to the results of forward flapping flight studies which are in the form of bird-like flight. In the fifth chapter the insect-like hovering results are given and discussed. The last chapter includes the conclusion of the present study.

CHAPTER II

LITERATURE SURVEY

The general intent to understand the nature's choices on the animal flight has led the biologist to investigate the aerodynamic mechanisms responsible for animal locomotion. On the other hand, the increasing military needs for surveillance and reconnaissance have led the engineers to design and build flapping wing micro aerial vehicles (MAV) in the last two decades. The meeting point of the two different communities has improved the cooperation and accelerated the studies to understand the unrevealed secrets of natural flyers and to be capable of mimicking them for building successive MAVs.

The increasing interest in the engineering community on flapping wing flight also shows itself in literature. For instance the AIAA Journal has offered a special issue as *Biologically Inspired Aerodynamics* (Vol.49, no: 9) and also there is a special issue of Experiments in Fluids as *Animal Locomotion: The Physics of Flying* (Vol.46, no: 5) in 2008 and 2009, respectively. Moreover several books are published in recent years on the flapping aerodynamics of natural flyers with an engineering aspect [6-13].

The present chapter is devoted to the experimental, numerical and analytical studies regarding the flapping wing aerodynamics in literature. The chapter is divided into two sections. In the first part, the studies based on forward flapping flight are listed. The second section includes the hovering studies which are mostly based on insect

flight since the birds cannot hover except hummingbirds which also use the same aerodynamic mechanisms with insects.

2.1 Forward Flapping Flight Studies

The initial studies on flapping wings are the independent works of Knoller [14] and Betz [15] in a century ago. In the two independent studied they observed that flapping motion of the airfoil induces effective velocity which result as an effective angle of attack history during the motion. The effective angle of attack thus generates an aerodynamic force on the airfoil that could be decomposed into lift and drag/thrust components. The capability of flapping wings to create thrust is called Knoller-Betz effect [16] and verified experimentally for the first time by Katzmayr [17].

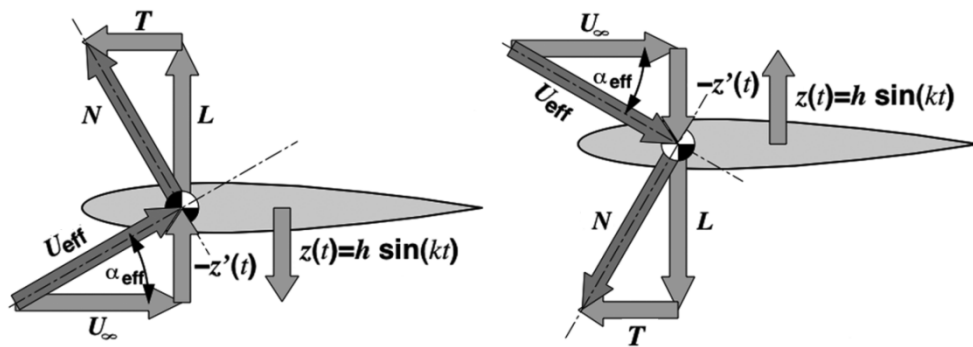


Figure 2.1 Effective angle of attack generation by flapping motion in a steady current [14].

The first numerical study on flapping airfoils is performed by Birnbaum using linearized potential flow theory in his dissertation [19]. Moreover, Birnbaum defined - the most important similarity parameter in flapping wing aerodynamics- reduced frequency (k) for the first time as,

$$k = 2\pi f c / U_{\infty} \quad (2.1)$$

where f is the flapping frequency, c is chord length and U_{∞} is the free stream velocity. The reduced frequency is the rate of flapping velocity to the free stream velocity and thus it is a kind of measure of flow unsteadiness imposed by flapping motion.

The first explanation of the thrust production is presented, after a decade of Birnbaum, by von Kàrmàn and Burgers [20]. They related the vortex shedding from the trailing edge as a momentum deficit or surplus in the wake of the airfoil. One other important study at these times is the Theodorsen's inviscid, incompressible analytical method [21] which is a suitable method for studying a wide range of flow conditions even now [22].

The advances in computational and experimental methods enable to study real viscous flows deeply. Recently, Pesavento and Wang [23] showed that the flapping flight can save up to 27% aerodynamic power compared to steady flight. They solved the Navier-Stokes equations on an elliptic airfoil it is found that the optimum flapping motion could be performed with less power compared to the optimal steady flight of the airfoil. This study cleared the doubts about the efficiency of flapping wing flight for manmade vehicles.

The initial studies on the pitching and plunging airfoils are mostly related with dynamic stall of the helicopter blades [24]. There exist plenty of reviews on dynamic stall in literature for which the Reynolds numbers are two orders of magnitude larger compared to MAV aerodynamics [25-28]. Moreover these studies generally use the most common helicopter blade profile, NACA 0012, for which the design Reynolds number is far beyond the operating Reynolds numbers of MAVs.

The birdlike flight studies are usually based on periodic motions to investigate the propulsive characteristics in cruise conditions rather than the non-periodic motions encountered during landing and take-off [29,30]. Most studies are seeking to find out

the best cruise conditions and configurations. For instance, Tuncer and Kaya [31] computed the flapping airfoils in biplane combinations and showed that with a proper phase shift the biplane configuration can produce 20-40% more thrust than a single airfoil. In further studies, Kaya et al. [32] optimized the amplitudes pitch and plunge motion and the phase shift between these motions for maximum thrust and propulsive efficiency of flapping airfoils in biplane configuration. It is showed the biplane configuration can be more efficient at a Strouhal number range of $0.17 < St < 0.25$ which agrees with natural flyers and swimmers [33]. In another study Tuncer and Kaya [34] performed parallel Navier-Stokes computations to optimize the propulsive efficiency of a single flapping airfoil. It is showed that the preventing the formation of the large scale Leading Edge Vortices (LEVs) augments the propulsive efficiency of single flapping airfoils.

Günaydinoğlu and Kurtuluş [35-38] studied the effect of Reynolds number, flapping kinematics, reduced frequency and airfoil geometry on unsteady aerodynamics of a flapping airfoil in forward flight. To achieve this, unsteady Reynolds-averaged Navier-Stokes equations coupled with Menter's Shear Stress Transport turbulence model are solved on deforming grids. The main motions are defined as pure plunge and pitch-plunge of the airfoil. It is observed that for both motions at all Reynolds number ranging from 10,000 to 60,000 dynamic stall of the airfoil is the main mechanism of lift production however the strength and duration of the leading edge vortex varies with airfoil geometry, reduced frequency. Moreover it is also showed that high force characteristics and favorable flowfields are achieved with higher reduced frequencies and low plunging amplitudes while keeping the Strouhal number constant. The computed flowfields are compared with the wide range of experimental studies and high fidelity simulations and concluded that the URANS solutions are applicable methods for investigating the flapping wing aerodynamics in forward flight.

2.2 Hovering Studies

The flapping motion of the birds and insects are more complex and advanced than manmade flyers could perform nowadays. McMasters and Henderson [39] state that humans fly commercially or recreationally, but animals fly professionally. The evolution of birds and insects on millions of years has taken them to a point in which current state of art cannot explain with a general theory. Nowadays a period like the first decades of the powered flight is being experienced to understand the complex bird and insect flight. The starting points to enlighten the topic are making assumptions to simplify this complex kinematics.

Freytmuth [40] emphasized that the mainstream studies on hovering motion are very animal specific and therefore very complex and hard to deeply investigate. Thus in his study, Freymuth defined simple generic hovering motions as a combination of pitching and plunging of a thin flat-plate with rounded edges. Three different hovering modes those mimic bird, insect and fish locomotion are defined as water-treading, normal hovering and oblique modes. The flowfields around the airfoils are visualized with titanium-tetra-chloride method and thrust coefficients are measured with Pitot tubes. It is concluded that the relatively simple hovering motions could produce large thrust coefficients. The vortical signature of the thrust generation is explained as reverse Karman vortex street.

The three dimensionality of the insect-bird flight is one of the main factors affecting on the complexity of the analyses. In her two independent studies, Wang showed that two dimensional computations are sufficient methods for investigating the three-dimensional flapping motions. In Reference [41] the aim is to seek for the optimal frequency for forward flight. To achieve this, vorticity-stream function form of Navier-Stokes equations are solved around a flapping ellipse which has the same flight conditions with a dragonfly in forward flight. It has been showed that the results totally agree with the three dimensional analysis of Hall et al. [42] in terms of

the optimal frequency. In other study of Wang [43] it is showed that two dimensional sinusoidal hovering could generate enough lift to support a typical insect weight. The same solution methodology is followed in this study and the dipole jet characteristics of forming vortices are showed for an ellipse undergoing figure-of-eight type hovering. These results also show that the general lift/thrust generating mechanisms in bird/insect flight are essentially two-dimensional and disagree with the former assumptions of Rayner [44] and Lighthill [45] which states that the generation of dipole vortices is a three dimensional effect.

Energetic point of view is also an attractive area in flapping flight studies. The natural flyers are evolved to fly in most efficient way for millions of years. Similarly it is aim to fly the manmade vehicles at most efficient conditions for which the energy sources are limited. To achieve this Berman and Wang [46] tried to optimize the kinematics of hovering insects. Three insects - fruitfly, bumblebee and hawkmoth - whose masses vary by three orders of magnitudes are analyzed. The morphological values of the insects are taken from previous experimental studies. A hybrid optimization procedure is followed to optimize the eleven flapping parameters with a quasi-steady model for fluid forces. The constraint of the optimization procedure is that the airfoil produces more lift than the weight of the insect. For all insects the optimized kinematics are figure-of-eight motions with different vertical translations amplitudes and different frequencies. Also it is showed that in each optimized kinematics the same leading edge is maintained throughout the strokes. It is concluded that the motion also uses passive wing rotation mechanisms in which the aerodynamic forces help to rotate the wing at the end of strokes, similar to the turning of a free-falling leaf.

Lehmann and Pick [47] studied the effect of vertical translation on the aerodynamic forces and moments produced by fruit fly wings that is performing clap-fling mechanism. Dynamically scaled electromechanical model is used to mimic the clap-fling motion of the hovering insect. They tested 17 kinematic patterns these are identical in horizontal amplitude, flapping frequency and geometric angle of attack history but different in vertical motion. It is concluded that the vertical for augmentation is largely independent of the forces produced due to the wing rotation

at the reversals and wake capture mechanisms. It also pointed out the pitching moments are strongly independent from the vertical force; however the two airfoil clap-fling mechanism increases the mean pitching moment nearly 21%. It has been very difficult to have force and moment measurements from experimental studies and this study also provides very useful data for computational studies as well as its results.

The highly maneuverability of the dragonfly is specially influenced with the four winged morphology of the insect. It has been shown that the mechanisms are wake capture and rotational circulation for the insects with such a small size [48]. Moreover Wang and Russell [49] studied the effect of the wing configuration of a hovering dragonfly on aerodynamic forces and power. They filmed a tethered dragonfly and acquired the wing kinematics of the forewing and hindwing. The obtained kinematics is then embedded into a two dimensional vorticity-stream function solver and aerodynamic forces and power consumption rates are computed. It is found that the out-of-phase motion of the wings consumes the minimum power to balance the weight of the insect. However the in-phase motion of the wings generates an extra force in vertical direction which could accelerate the insect. It is thought that the out-of-phase motion is used in steady hovering whereas the in-phase motion is used at the takeoffs.

At the moment of time being it is known that the animal flight could not be explained by conventional aerodynamic theory. In their study, Dickinson et al [48] used mechanical model of dragonfly to investigate the unsteady mechanisms responsible for lift generation such as delayed stall, wake capture and rotational circulation. The delayed stall is the unsteady mechanism in which a vortex generated on the leading edge of the airfoil and creates a suction side on the upper side of the airfoil at translation. It is known that the leading edge vortex (LEV) is stabilized with the existence of axial flow [50-52]. Wake capture and rotational circulations are the unsteady mechanism these occur at the stroke reversals due to the rapid angle change. These two mechanisms are found to be responsible for the two force peaks in the rotational lift history which are resulting by the fluid-structure interaction

Günaydinoğlu and Kurtuluş [53,54] studied the effect of vertical translation and Reynolds number on hovering aerodynamics via solving the incompressible, constant property Navier-Stokes equations around an airfoil undergoing figure-of-eight type hovering. It is observed that with increasing vertical translation amplitude the vortices become stronger and the formation of leading edge vortex is pushed towards the midstroke. However the mean lift values are not increasing proportionally with the vertical translation amplitude, the most efficient value is at the $Y=0.5$. In Reference [44] the effect of Reynolds number on mean forces are studied. The mean forces at eleven different Reynolds numbers are given. It is observed that both of the mean forces converge to a certain Reynolds number. The most preferable Reynolds number regime for the hovering airfoil in symmetric figure-of-eight motion is found as $Re=2000$ lower than the Reynolds number at which the mean forces converged.

CHAPTER III

NUMERICAL METHOD

The entire study includes different Reynolds number regimes ranging from very low to moderate Reynolds numbers. In forward-flapping cases where the Reynolds number is in the order of ten-thousands, the transition to the turbulence is crucial so the unsteady, incompressible Reynolds-Averaged Navier-Stokes equations coupled with Menter's Shear Stress Transport (SST) turbulence model are solved. On the other hand, in hovering cases which are performed at very low Reynolds numbers the flow is assumed fully laminar and therefore the unsteady, incompressible Navier-Stokes equations are solved. The different nature of forward flapping and hovering flight also differ in not only the governing equations but also the solution strategy, grid generation and vortex dynamics that will be explained in the following sections. Throughout the study commercially available CFD solver Fluent 6.3.26 is used on moving and deforming O-type grids with finite-volume methods [55].

3.1 Governing equations

The governing equations in hover are the incompressible, two-dimensional, constant property Navier-Stokes equations with the continuity equation are given as follows,

$$\frac{\partial}{\partial x_i}(u_i) = 0 \quad (3.1)$$

$$\frac{\partial}{\partial t}(u_i) + \frac{\partial}{\partial x_j}(u_j u_i) = -\frac{1}{\rho} \frac{\partial p}{\partial x_i} + \nu \frac{\partial^2}{\partial x_j^2} \{u_i\} \quad (3.2)$$

where x_i is the i^{th} component of position vector, u_i is the velocity component in i^{th} direction, t is the time, ρ is the density, p is the pressure and ν is kinematic viscosity.

The governing equations for forward-flight are Unsteady Reynolds-Averaged Navier-Stokes equations coupled with Menter's Shear Stress Transport (SST) turbulence model. The URANS equations with continuity equation for incompressible, two-dimensional flow are as follows,

$$\frac{\partial}{\partial x_i}(u_i) = 0 \quad (3.1)$$

$$\frac{\partial}{\partial t}(u_i) + \frac{\partial}{\partial x_j}(u_j u_i) = -\frac{1}{\rho} \frac{\partial p}{\partial x_i} + \frac{\partial}{\partial x_j} \left\{ (\nu + \nu_t) \frac{\partial u_i}{\partial x_j} \right\} \quad (3.2)$$

$$\frac{\partial k}{\partial t} + \frac{\partial}{\partial x_j}(u_j k) = \frac{\tau_{ij}}{\rho} \frac{\partial u_i}{\partial x_j} - \beta^* \omega k + \frac{\partial}{\partial x_j} \left\{ (\nu + \sigma_k \nu_t) \frac{\partial k}{\partial x_j} \right\} \quad (3.3)$$

$$\begin{aligned} \frac{\partial \omega}{\partial t} + \frac{\partial}{\partial x_j}(u_j \omega) &= \frac{\gamma}{\nu_t} \frac{\tau_{ij}}{\rho} \frac{\partial u_i}{\partial x_j} - \beta \omega^2 + \frac{\partial}{\partial x_j} \left\{ (\nu + \sigma_\omega \nu_t) \frac{\partial \omega}{\partial x_j} \right\} \\ &+ 2(1 - F_1) \sigma_\omega \frac{1}{\omega} \frac{\partial k}{\partial x_j} \frac{\partial \omega}{\partial x_j} \end{aligned} \quad (3.4)$$

$$\nu_t = \frac{a_1 k}{\max(a_1 \omega; \Omega F_2)} \quad (3.5)$$

$$\tau_{ij} = \rho \nu_t \left(\frac{\partial u_i}{\partial x_j} + \frac{\partial u_j}{\partial x_i} \right) - \frac{2}{3} \rho k \delta_{ij} \quad (3.6)$$

where k is the turbulent kinetic energy, ω is the specific dissipation rate, ν_t is eddy viscosity, Ω is the absolute value of vorticity, δ_{ij} is the kronecker delta and τ_{ij} is the stress tensor. a_1 , σ_ω , σ_k , β , β^* are the modeling constants in Menter's SST formulation [56]. F_2 and F_1 are the blending functions which allows switching between $k - \omega$ model near solid boundaries and $k - \varepsilon$ model out of the boundary layer. It has been shown that Menter's SST formulation stands as the most advanced two-equation turbulence model in the prediction of adverse pressure gradient flows [57].

Throughout the entire study the mass of the airfoil is ignored. Moreover, the working fluid is chosen as air and the body force term is dropped from the governing equations. These set of equations are solved on moving and deforming two-dimensional grids with the pressure-based finite volume solver. The dynamic mesh feature of the code restricts us to use first order implicit schemes for temporal discretization. On the other hand, convective and diffusive terms are treated using second-order accurate schemes. The pressure and velocity coupling is handled by SIMPLE algorithm [58].

3.2 Computational Grid and Boundary Conditions

The prescribed motions for forward-flight and hover cases are implemented via different mesh moving strategies. In forward flight cases the grid domain is divided into two parts as inner grid and outer grid. The inner grid is the domain which is not deforming and moving as a rigid body with the airfoil. On the other hand, the outer part is the deforming part which is modeling the velocity inlet and pressure outlet boundary conditions. In hovering cases since there is no free-stream velocity, the whole grid is moving with the airfoil and the outer surfaces of the grid domain is imposed as pressure-outlet boundary condition. In all studied cases the airfoil surface has no-slip wall boundary condition. The motions are implemented to the code via User Defined Functions (UDF) in which the axial and rotational velocities of the rigid body around a pivot point are the inputs.

In the thesis the main geometry is chosen as SD7003 airfoil for which the design Reynolds number is in the limit of 50,000 and 100,000. The excessive work done with SD7003 airfoil in the literature for forward flapping flight also gives chance to validate the present solutions with experimental studies. The substitutional geometry is flat-plate with 2.5% thickness with rounded edges. In the case of flat-plate there will be no pressure gradient arising from the model geometry. Hence flat plate studies stand as a fundamental study and that will lead us to observe more aggressive dynamic stall.

Figure 3.1 shows the unstructured grid domain around the SD7003 airfoil that is used in forward flight cases. The first cell on the airfoil surface has a wall y^+ value of 1 and there are 20 grid points normal to the flow direction to resolve the boundary layer. The whole grid has about 85,000 cells which is found as adequate to have grid independent solution. The total grid has 60 chords diameter where the inner grid has a diameter of 30 chords.

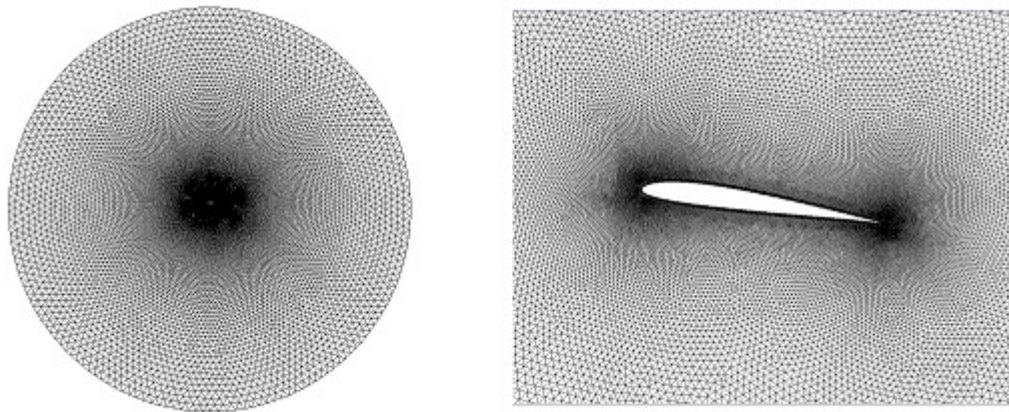


Figure 3.1 Unstructured grid around SD7003, in open bounded domain (left) and its distribution near airfoil (right).

Figure 3.2 shows the unstructured grid around the flat plate with rounded edges. This grid is used to observe the effect of airfoil geometry by comparing the forward flight solutions with SD7003 cases. Hence same with SD7003 case, the first cell on the airfoil surface also has a wall y^+ value of 1. There are 20 grid points normal to the flow direction in the boundary layer. The grid has about 67,000 cells that is also shown adequate to have grid independent solution. The flat plate geometry also gives a chance to generate structured grid around the geometry easily. On the other hand the code itself is only capable of deforming unstructured grids. Unstructured grids are generated not only in outer grid, but also in the inner grid. The total grid has a diameter of 60 chords where the inner grid is a circle with a diameter of 30 chords.

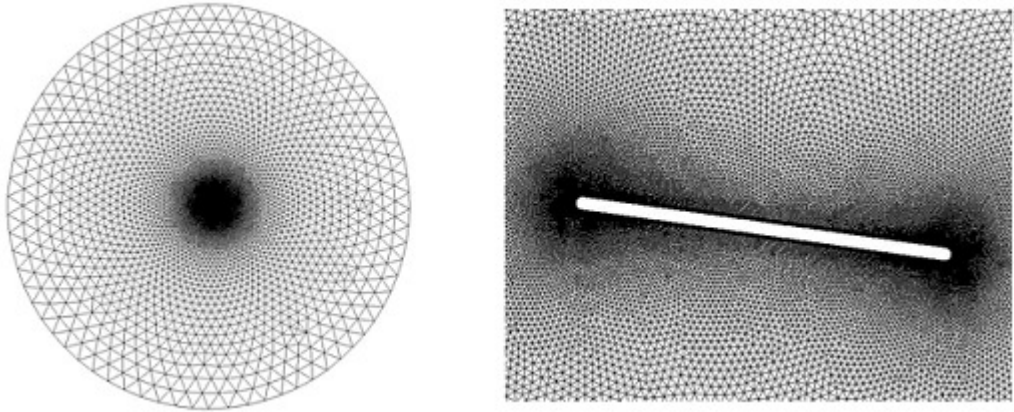


Figure 3.2 Unstructured grid around flat-plate, in open bounded domain (left) and its distribution near the flat plate (right).

Figure 3.3 shows the structured grid around SD7003 airfoil that is used for hovering cases. Since the whole grid domain is moving as a rigid body in hovering cases, there is no need to generate unstructured grid domain. A structured grid, which allows having fewer elements than an unstructured grid, is generated with elliptic grid generator GRIDGEN. After grid refinement studies 199x100 elements are found adequate to have grid independent solution for hovering cases. The O-grid has a total diameter of 30 chords which has the same diameter with the inner grids of forward flight cases.

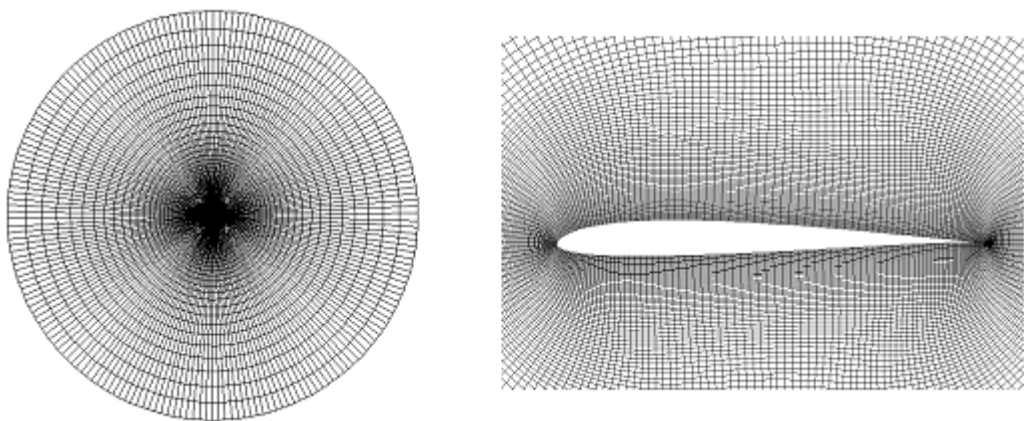


Figure 3.3 Structured grid around SD7003 airfoil, in open bounded domain (left) and its distribution near airfoil (right).

3.3 Grid and Time-step Refinement Study

In all cases to assess a grid and time-step independent numerical solutions, refinement studies are carried out. Figure 3.4 shows the grid and time-step refinement studies for hovering cases in terms of lift and drag coefficients over three periods of motion. For grid independence test, two O-type structured grids with 199x100 and 399x200 elements are used in hovering mode. The results are given in Figure 3.4 (left) and it is found that 199x100 elements are adequate to have grid independent solution. The time-step independence study is performed for three different values such as 200, 400 and 800 time-steps (Δt) over one period (T) of motion. As it can be seen in Figure 3.4 (right), 400 time-steps over one period of motion could be used for further studies. In hovering cases, the lift and drag forces denote the vertical and horizontal components of the net force on the airfoil. Hence the extreme value of drag force, with respect to conventional fixed-wing aerodynamics, could be explained by that sign convention.

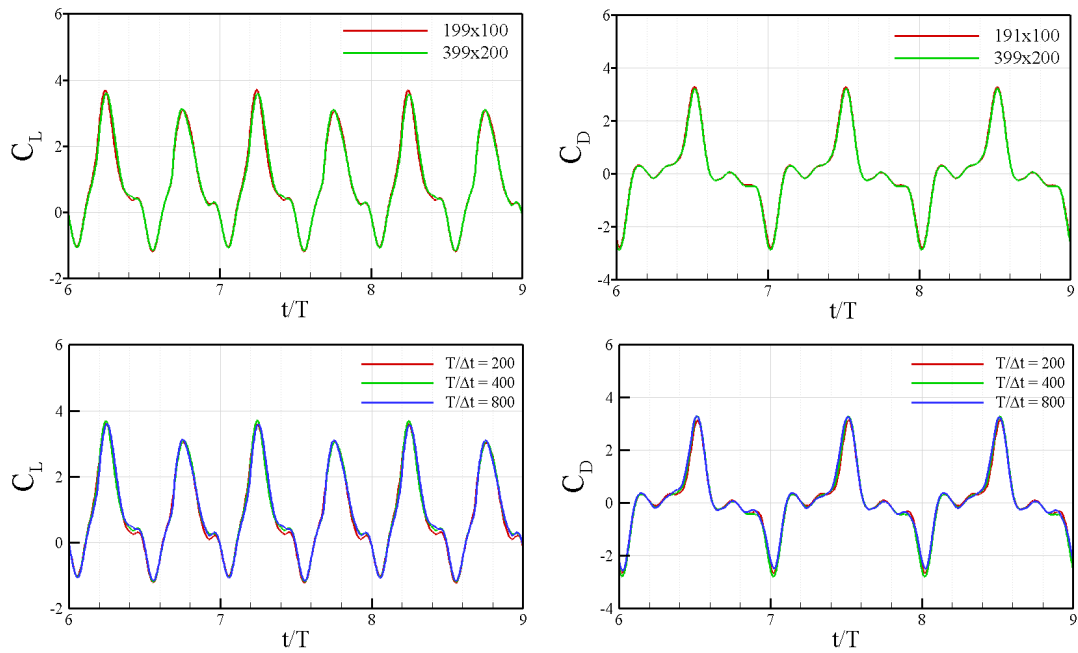


Figure 3.4 Time histories of lift and drag coefficients with different grids (top) and with different time-steps (bottom) in hover for three periods of flight.

Figure 3.5 shows the grid refinement study for the forward flapping cases around SD7003 airfoil (left) and around flat plate (right). It is found that above 85000 cells the solution around SD7003 is not altering much and a grid with that many cells is appropriate to have grid independent solution in forward flight cases. Moreover, time independent solutions for flat plate studies are obtained with 67000 cells. 960 time-steps over one period of motion is used for forward flight cases. The resulting grids are showed in Figure 3.1 and 3.2.

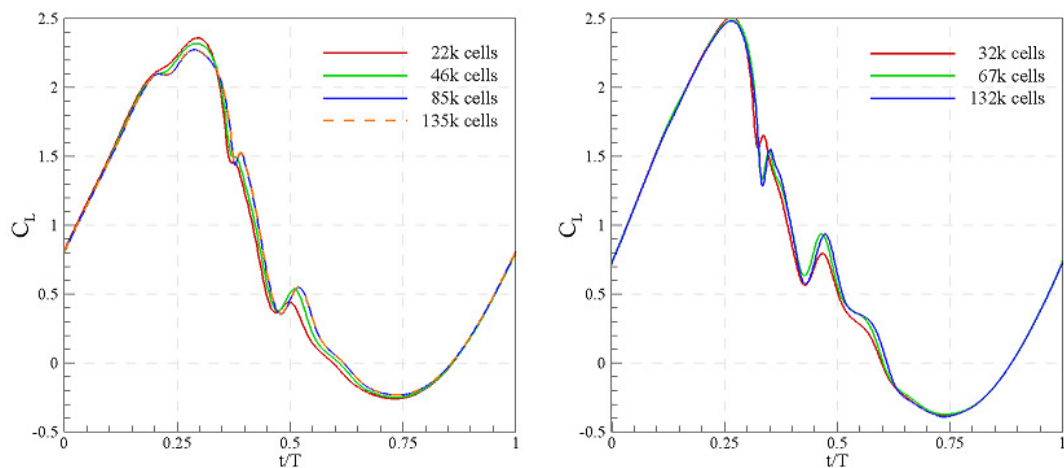


Figure 3.5 Time histories of lift coefficient history with different grids around SD7003 (left) and flat plate (right).

3.4 Forward flight kinematics

The flapping motion in forward flight described as pure plunging or the combination of plunging with pitching around a pivot point. The plunging is described as the motion of the airfoil normal to the free-stream without any change in geometric angle of attack. On the other hand, the pitching is described as the rotation of the airfoil with respect to a pivot point. The pivot point, rotation center, is chosen as the quarter chord throughout the study. The flapping motion in the existence of a free stream velocity is defined by,

$$h(t) = h_0 c \cos(\omega t) \quad (3.9)$$

$$\alpha(t) = A \cos(\omega t + \pi/2) + \alpha_0 \quad (3.10)$$

where $h(t)$ is the instantaneous horizontal position of airfoil, $\alpha(t)$ is the geometric angle of attack of the airfoil. h_0 is non-dimensional plunging amplitude and A is pitching amplitude in degrees, ω is circular frequency ($\omega = 2\pi f$), where f is the physical frequency, α_0 is the mean angle of attack, c is the chord and $\pi/2$ stands as a phase shift between pitching and plunging motions.

3.5 Hovering kinematics

In hovering cases, “figure-of-eight” motion that has three degree of freedom, is implemented (See Figures 5.1 and 5.2). The figure-of-eight hovering motion is defined by,

$$x(t) = 2c \sin(\omega t + \pi/2) \quad (3.11)$$

$$y(t) = Yc \sin(2\omega t) \quad (3.12)$$

$$\alpha(t) = \pi/2 + \pi/2 \sin(\omega t) \quad (3.13)$$

where $x(t)$ and $y(t)$ are instantaneous horizontal and vertical coordinates of the pivot point in inertial frame of reference. Y is the amplitude of vertical translation of the airfoil. The flapping path of the airfoil, which results from these set of parametric sinusoidal equations, is defined as Lissajous curve. The coefficients of ωt term in Equations 3.11 and 3.12 and the phase shift between the horizontal and vertical motion of the airfoil determines the general shape of Lissajous curves – figure of eight shape in the present study. The coefficients in front of the sine functions in Equations 3.11 and 3.12 do not alter the general figure of eight pattern but alter the amplitudes of the vertical and horizontal translations.

3.6 Significant non-dimensional parameters

In flapping wing aerodynamics two non-dimensional similarity parameters, those have significant role regarding to the flow dynamics, are Reynolds number (Re) and reduced frequency (k). The reduced frequency is the ratio of vertical velocity to the axial velocity. For plunging airfoils the term relates the flapping velocity to the free stream velocity and signifies the flapping frequency. The definitions of Reynolds number and reduced frequency are given by Equations 3.14 and 3.15, respectively.

$$Re = U_{ref}c/v \quad (3.14)$$

$$k = \omega c / (2U_{ref}) \quad (3.15)$$

In forward flight cases the free stream velocity (U_∞) is used as reference velocity. On the other hand in hovering cases the reference velocity is defined by the maximum velocity and given by Equation 3.16.

$$\begin{aligned} U_{ref} &\stackrel{\text{def}}{=} \sqrt{\dot{x}(t)^2 + \dot{y}(t)^2 + \left(\frac{\dot{\alpha}(t)c}{4}\right)^2} \Big|_{max} \\ &= 2\omega c \sqrt{1 + Y^2} \end{aligned} \quad (3.16)$$

In hovering cases, since no free stream velocity exists, the reduced frequency is defined as the ratio of maximum vertical velocity to the maximum horizontal velocity. In the present study, the horizontal velocity of the airfoil is kept same for all hovering cases. Therefore the amplitude of horizontal translation is also constant for all hovering cases and the resulting value of reduced frequency is only dependent to the vertical translation amplitude. The definition of reduced frequency for hovering cases is defined by Equation 3.17.

$$k \stackrel{\text{def}}{=} \frac{1 \max(\dot{y})}{2 \max(\dot{x})} = 2\omega cY / 4\omega c = Y/2 \quad (3.17)$$

CHAPTER IV

FORWARD FLIGHT RESULTS

In this chapter, the results of principally two different flapping motions, pure plunging and combined pitching and plunging, are introduced within the existence of free stream velocity. The effects of reduced frequency, Reynolds number and airfoil shape are investigated. The following results are compared with the experimental studies of NATO AVT-149 Micro Air Vehicle Unsteady Aerodynamics Task Group [22].

4.1 Baseline Motion and Related Parameters

The baseline flapping cases are pure plunge and combined pitch-plunge motions at Reynolds number of 60000 for reduced frequency of 0.25. The motion in consideration is given by Equations 4.1 and 4.2. For plunge motion the pitching amplitude, A , is equal to zero. For combined pitch-plunge motions A is taken as 8.43° .

$$h(t) = 0.5c \cos(\omega t) \quad (4.1)$$

$$\alpha(t) = A \cos(\omega t + \pi/2) + 8^\circ \quad (4.2)$$

The general principal of thrust generating of plunging motion is that plunging induces a relative velocity normal to the free stream velocity. That induced velocity generates an effective angle of attack as a function of time and the airfoil faces the

air with that angle of attack despite of the geometric angle of attack. This is the same phenomenon as the downwash velocity at the tips of finite wings. The tip vortices induce downwash velocity and that normal velocity alters the angle of attack of the wing, hence the forces on the wing. The effective angle of attack of the airfoil as a function of time is given by Equation 4.3,

$$\alpha_{Eff}(t) = \alpha(t) - \tan^{-1} \left(\frac{\dot{h}(t) + 0.25c\dot{\alpha}(t) \cos(\alpha(t))}{U_{\infty} - 0.25c\dot{\alpha}(t) \sin(\alpha(t))} \right) \quad (4.3)$$

The pitching motion of the airfoil is defined about quarter chord throughout the study. The 0.25 in the above equation is the distance between the leading edge of airfoil and the pivot center. In Equation 4.3 the effective angle of attack is defined relative to the leading edge of the airfoil. Since the leading edge of the airfoil is $c/4$ away from the pivot point, the effective angle of attack also includes that effect which is known as *pivot effect*.

Figure 4.1 shows the variations of geometric and effective angle of attack with time for pure plunge and combined pitch-plunge motions at $Re=60000$ and $k=0.25$. The green dashed line shows the time history of the geometric angle of attack for the airfoil during combined pitch-plunge motions. The geometric angle of attack for plunge motion is constant and equal to 8° over the period. The red and blue dashed lines are denoting the effective angle of attack over whole period for pure plunge and combined pitch-plunge motions, respectively. The solid black line is the effective angle of attack with the pivot effect for combined pitch-plunge motion. The maximum effective angle of attack for pure plunge motion is 22.4° and for combined pitch-plunge motion it is 14.04° . In both cases the maximum effective angle of attack is greater than the static stall of the SD7003 airfoil, i.e. 11° . There is slight difference between time histories effective angle of attack with and without pivot effect for these cases. This difference will increase with increasing reduced frequency, i.e. pitching frequency. The same motion is also investigated for high reduced frequency and that effect is shown in upcoming sections. One other parameter that affects the pivot effect is the location of pivot point. Increasing the non-dimensional distance

between the leading edge and the pivot point increases the pivot effect. In all investigated cases throughout the thesis the pivot point is chosen as the quarter chord.

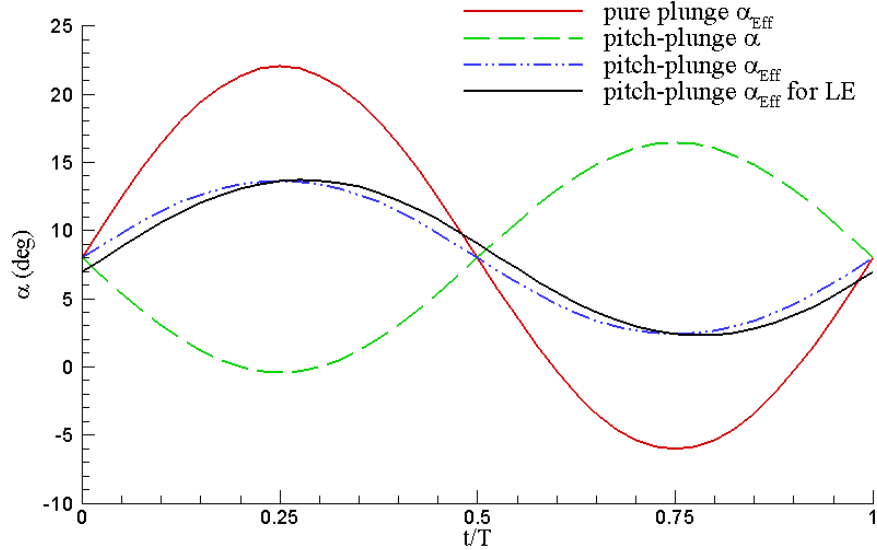


Figure 4.1 Time histories of geometric and effective angle of attack over one period of pure plunge and combined pitch/plunge motions at $Re=60000$ and $k=0.25$.

All investigated cases for forward flight studies are reported in Table 4.1. The pitching (A) and plunging (h_0) amplitudes are defined by in Equations 3.9 and 3.10. The low reduced frequency cases are also studied around flat plate at $Re=60,000$ to investigate the effect of geometry on instantaneous velocity and vorticity fields and aerodynamic forces and moments. To balance the Strouhal number between the high frequency and low frequency cases, the plunging amplitude is decreased to 0.05 for cases with reduced frequency of 3.93. Plugging these values gives the Strouhal number for low frequency cases as $St=0.08$ and for high reduced frequency cases it is $St=0.125$

Table 4.1 Investigated parameters for forward flight cases of SD7003 and flat plate.

Cases	k	α_o	h_o	A	$Re (x10^3)$
Pure plunge	0.25	8	0.5	0	10, 30, 60
Pitch-plunge	0.25	8	0.5	8.43	10, 30, 60
Pure plunge	3.93	4	0.05	0	60
Pitch-plunge	3.93	4	0.05	8.43	60

4.2 Pure Plunge Case

The pure plunge case is the fundamental motion in forward flight cases. Figure 4.2 shows the contours of instantaneous streamwise component of velocity for seven different phases of motion. The streamwise velocity component is normalized with free stream velocity. The results of the computations are showed on the left column, the PIV solutions of Air Force Research Laboratory [22] are shown in the middle column whereas the solutions on the last column is the URANS computations of Michigan University [22]. In experimental results the laser reflects from the pressure side of the airfoil so there is not any reliable data at that regions. The same region is also taken out in URANS computations. Moreover Fig. 4.3 shows the out-of-plane component of vorticity with the same order of Figure 4.2. This time the vorticity is normalized with free stream velocity and chord length. The near zero values for vorticity are blanked to have a clear view. The force coefficient histories for that motion are given in Figure 4.3 with comparison of several studies in AVT-149.

The deep dynamic stall of the airfoil could be expected by examining the effective angle of attack variation during the motion. The maximum value of effective angle of attack is two times larger than the static stall of the SD7003 airfoil. The flow remains attached at the beginning of motion where the effective angle of attack is 8° . At approximately $t/T=0.05$ the airfoil exceeds the static stall limit and a clockwise rotating leading edge vortex (LEV) starts to form. The LEV has its maximum dimension at $t/T=0.333$. The generation of vortex creates a suction region on the

suction side of the airfoil. The growing LEV is the reason of the increasing lift trend of the airfoil up to $t/T=0.333$ that could be observed in Figure 4.4. After that time the free stream is washing the LEV out and the lift is following a decreasing trend up to $t/T=0.75$. Following the minimum lift at $t/T=0.75$ the lift is again increasing with increasing effective angle of attack. Most of the lift during the motion is supplied at the downstroke. At $t/T=0.5$ a massive separation is observed in both results. Rather than the experimental study, a counter clockwise rotating vortex is observed in numerical studies at $t/T=0.25$.

There is an agreement with the experimental and numerical results in terms of vortex field and velocity distribution. One discrepancy occurs at the beginning of the LEV generation ($t/T=0.25$) in URANS solutions of Michigan University. In other solutions the separated LEV could be observed at that time instant where in that study LEV is just growing. That discrepancy also be observed in lift time history. The experimental study is composed of phased-averaged data so vortex field in numerical airfoil starts to generate the next LEV of the new period. At $t/T=0.417$ a counter clockwise (CCW) rotating trailing edge vortex (TEV) grows, and that vortex detaches from the airfoil surface very quickly. The trace of the detached vortex could be observed in Figure 4.3 at $t/T=0.5$. TEV is found as stronger than other results ($t/T=0.417$).

In Figure 4.4 the solutions are compared with experimental and numerical studies this time including two-dimensional and three-dimensional Large Eddy Simulations (LES). The present computation agrees well with LES solutions. The Theodorsen's analytical solution is also comparable in that deep stall case especially at the first and last quarters of the motion where the lift follows a relatively smoother trend. The computations are the closer solution to the 3D LES solutions and 2D PIV experiment. The lift is roughly in a sinusoidal trend whereas the drag is not closer to any kind of smooth curve. The drag for present computations shows a very well agreement with the 3D LES solutions of AFRL even better than 2D LES solutions. The blue line also denotes 2D LES solutions of National Research Council of Canada (NRC) [60] and it underpredicts the drag due to LEV formation. The drag time

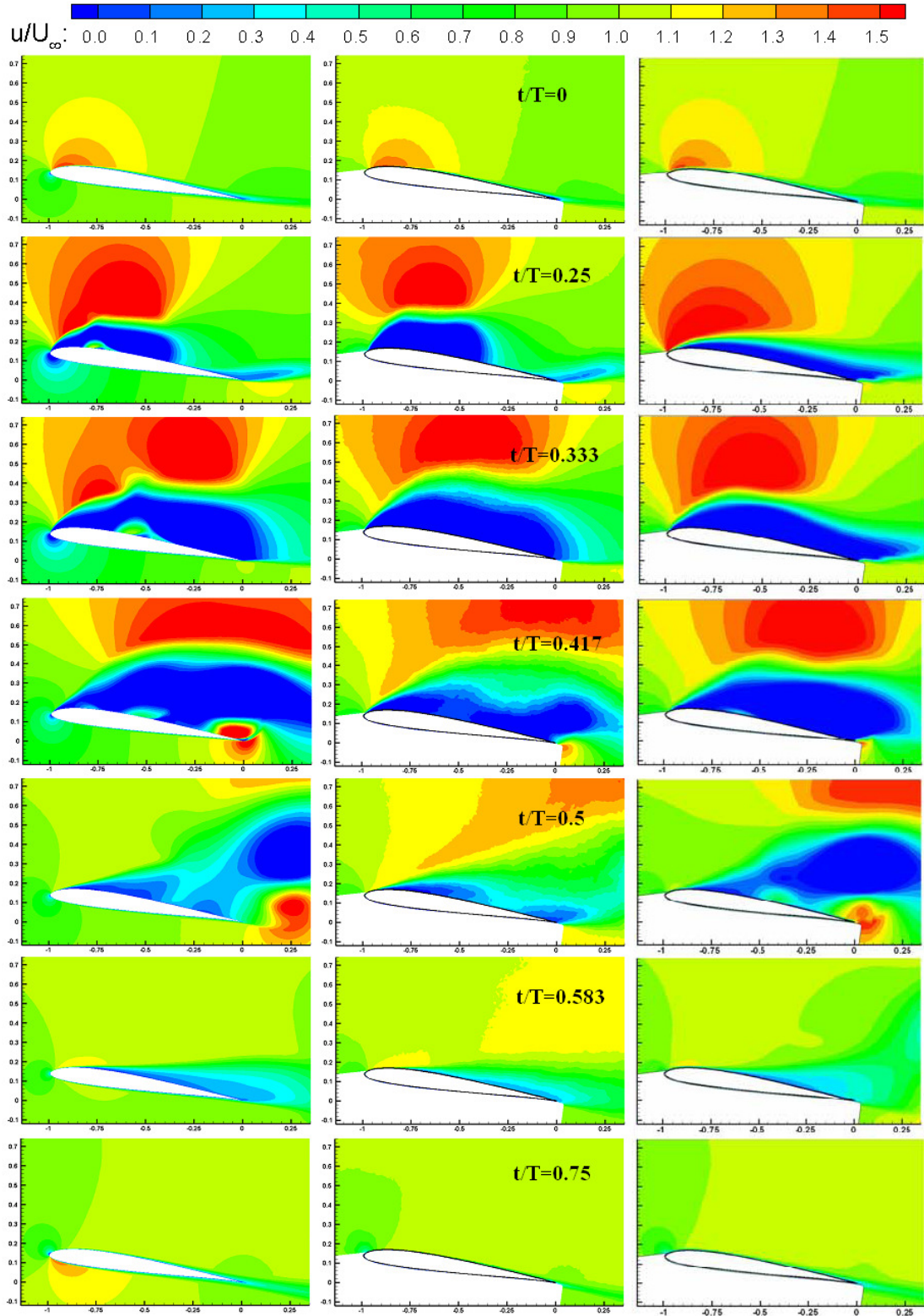


Figure 4.2 Normalized u-velocity contours from present computation (left column), PIV experiment of AFRL (middle column) and URANS solution of Michigan University (right column) for pure plunge, $Re=60,000$ $k=0.25$ [22].

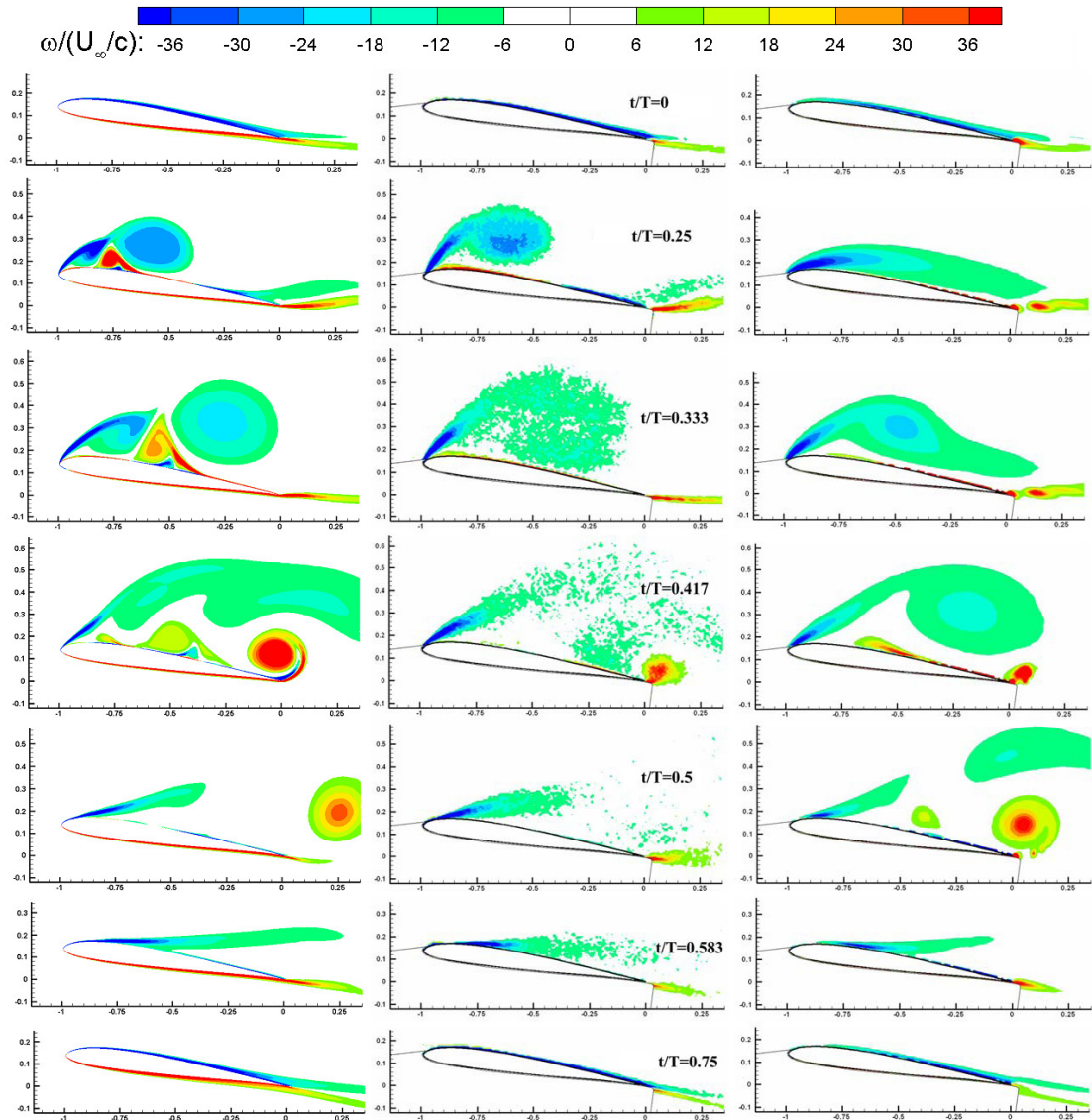


Figure 4.3 Normalized out-of-plane component of vorticity contours from present computation (left column), PIV experiment of AFRL (middle column) and URANS solution of Michigan Uni. (right column) for pure plunge, $Re= 60000$, $k=0.25$ [22]. studies are smoother. During the upstroke the boundary layer reattaches and the

history agreement of 3D LES and present solutions are in terms of the similar vortex field results of the two studies. The drag is much more sensitive to errors because of its relatively smaller quantity.

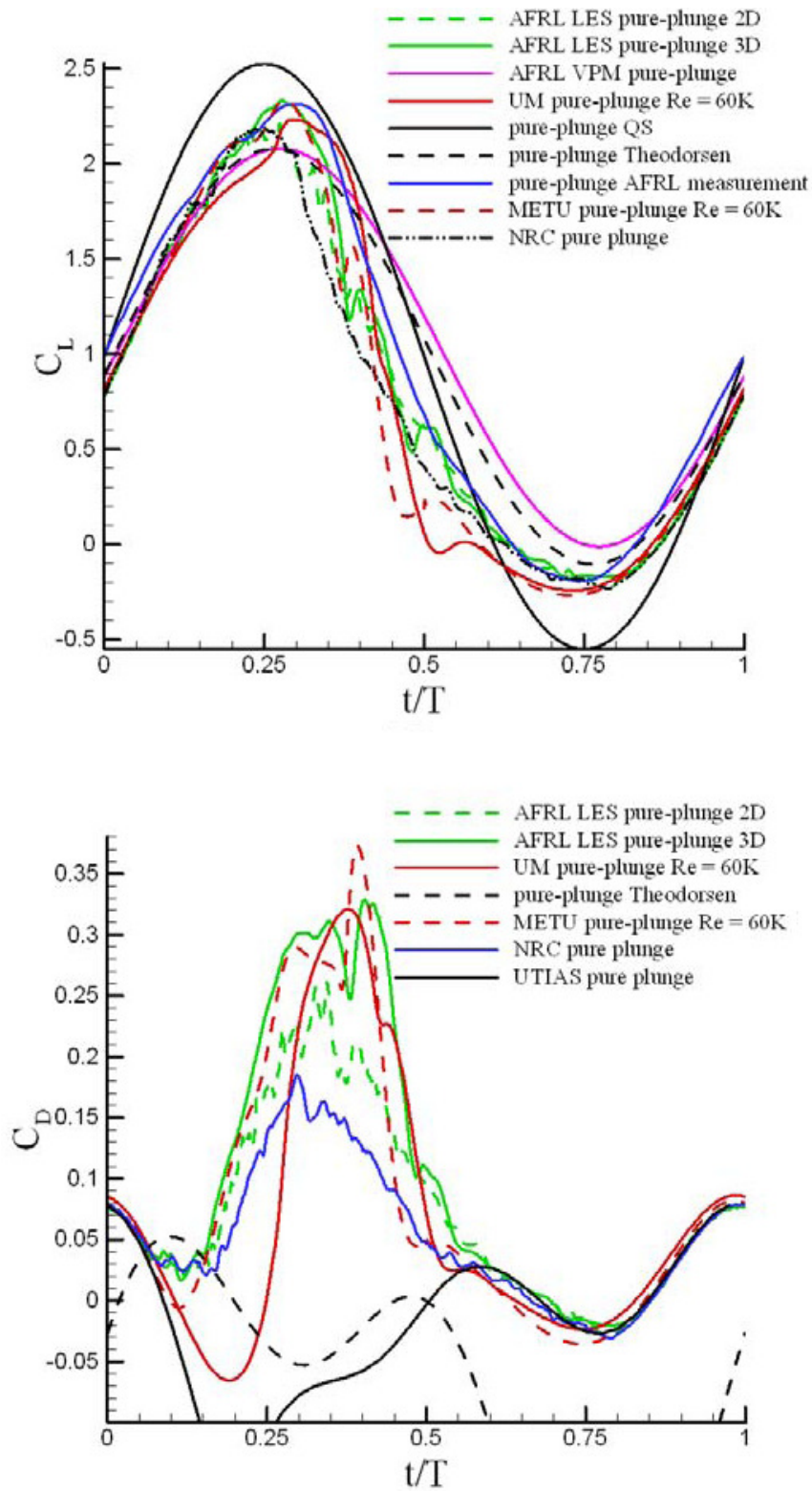


Figure 4.4 Time histories of lift coefficient (top) and drag coefficient (bottom) for pure plunge motion at $Re=60000$ and $k=0.25$. The results of this work are reported as METU results in Ref. [22].

4.3 Combined Pitch-Plunge Case

The combined pitch-plunge case is a shallow dynamic stall case where the maximum effective angle of attack is 14° over the period. The Reynolds number is again 60000 and the reduced frequency is 0.25. The time history of effective angle of attack is sinusoidal similar to the pure plunge case but this time a smaller LEV formation expected at $t/T=0.25$. Figure 4.3 shows the streamwise velocity contours for four different phases from two PIV experiments from TU Braunschweig (TUBS) and AFRL. The middle column solutions focus on the boundary layer resolution and the transition point so eleven different PIV windows are used. Figure 4.6 show the normalized vorticity contours of the same solutions in Figure 4.5. Figure 4.7 compares the lift and drag coefficient history with available experimental and numerical results.

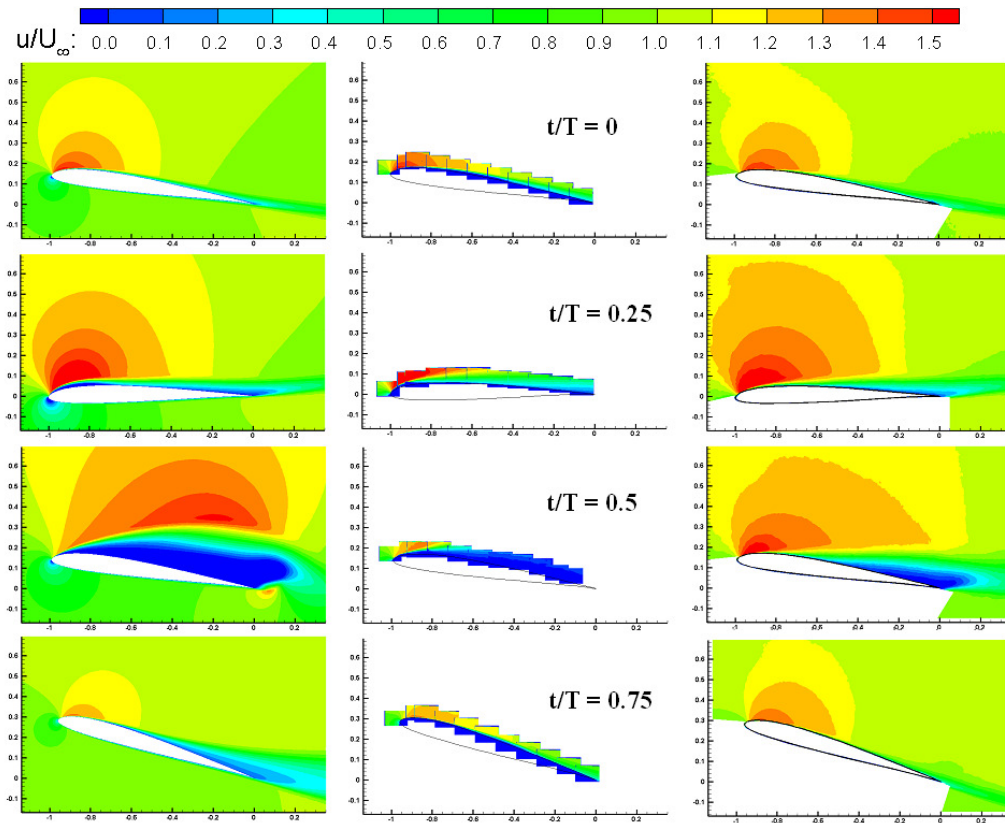


Figure 4.5 Normalized u -velocity contours from present computation (left column), PIV experiment of TU Braunschweig (middle column) and PIV experiments of AFRL (right column) for combined pitch-plunge, $Re=60000$ $k=0.25$ [22].

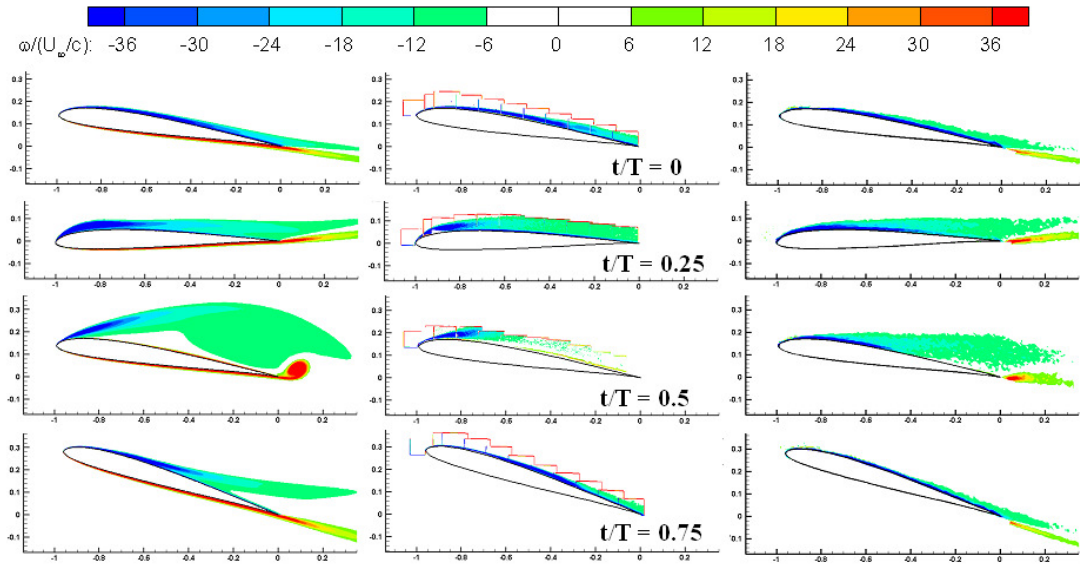


Figure 4.6 Normalized out-of-plane component of vorticity contours from present computation (left column), PIV experiment of TU Braunschweig [22] (middle column) and PIV experiments of AFRL [22] (right column) for combined pitch-plunge, $Re=60000$ $k=0.25$.

At the beginning of the motion at $t/T=0$ the effective angle of attack is 8° all results seem similar without any separation. At $t/T=0.25$ the effective angle of attack reaches its maximum value of 13.6° and onset of separation is observed at that time instant. The similar behavior is also observed in TUBS results (middle column) in Figure 4.5 and 4.6. At end of the downstroke the LEV separates from the upper surface of airfoil. At that time instant a TEV is also observed where the effective angle of attack is smaller than the static stall of the airfoil. The present study shows LEV formation during the downstroke as TUBS results whereas the AFRL PIV experiment shows only small separation. In pure plunge case the LEV is formed in the first quarter of the motion, but in this motion the LEV formation is delayed to the second quarter of the period. That observed LEV formation is the reason of the deep crests in Figure 4.7 with respect to experimental and other numerical studies. All other solutions are again in a sinusoidal-like trend but that time there is not a general consistency. The shallow stall case is more sensitive to the differences in numerical and experimental methods and the approaches to turbulence modeling.

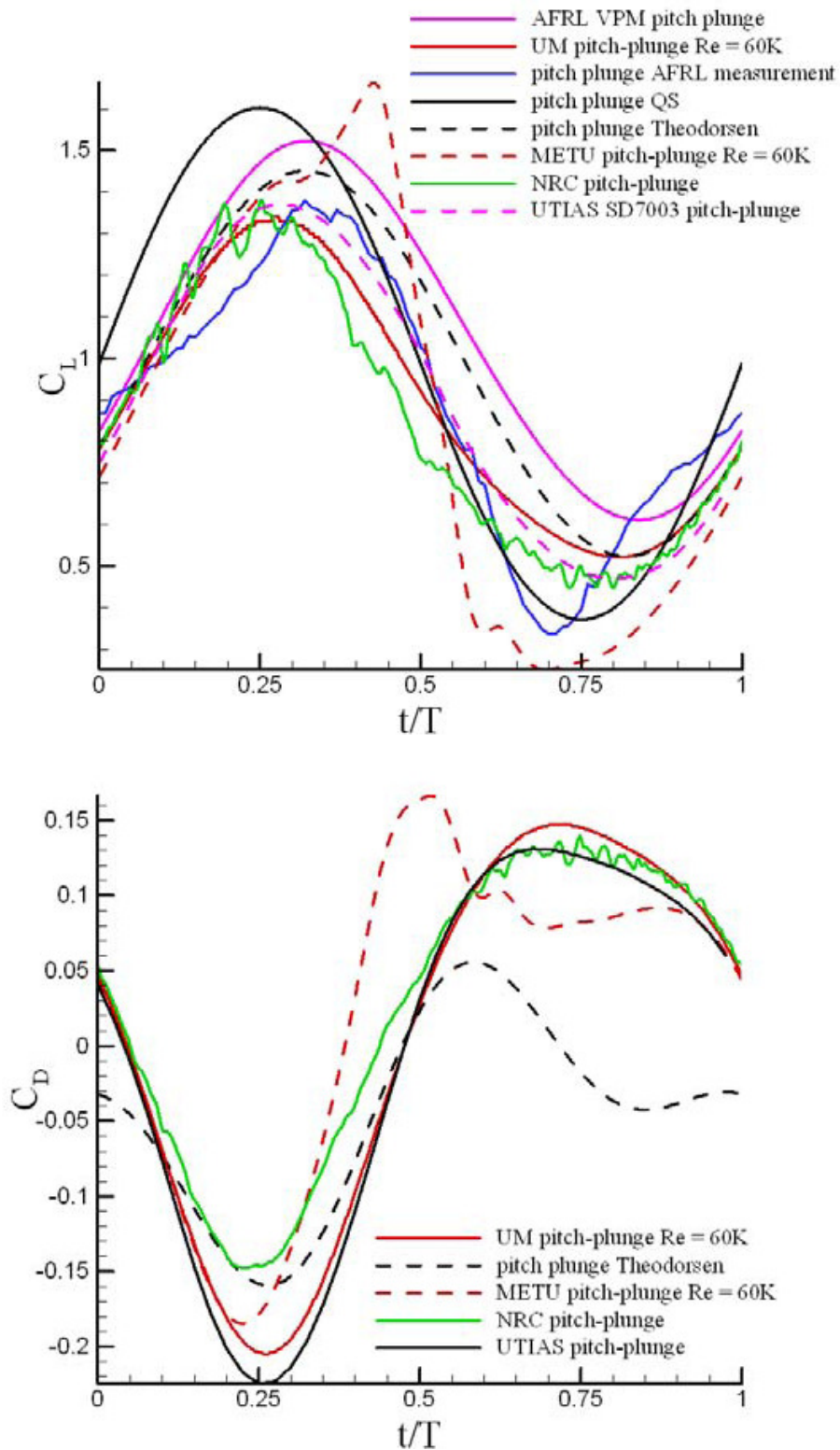


Figure 4.7 Time histories of lift coefficient (top) and drag coefficient (bottom) for combined pitch-plunge motion at $Re=60000$ and $k=0.25$. The results of this work are reported as METU results in Ref. [22].

4.4 Effect of Airfoil Geometry

The pure plunge and combined pitch-plunge motions at $Re=60000$ and $k=0.25$ are also studied for flat plate with thickness of 3%. The edges of the flat plate are rounded in that study and the sharp leading edge forces towards separation. The sharp leading edge arises the expectations of having massive separation even in shallow dynamic stall case. Figure 4.8 shows the normalized vorticity contours for combined pitch-plunge motions at $Re=60000$ and $k=0.25$ and Figure 4.9 shows the normalized vorticity contours of pure plunge motion for six phases. The flat plate itself is not introducing pressure gradient and could be seen as a more fundamental case than the airfoil.

The present computations agree well with the experiments for every phase of the combined pitch-plunge motion with flat plate (Figure 4.8). At $t/T=0$ the flow is not fully attached as SD7003 case (Figure 4.6). This time in all solutions the onset of the LEV formation could be observed. This formation is observed at $t/T=0.25$ in SD7003 case. At $t/T=0.25$ the LEV could be seen in all studies which separates the airfoil suction side before $t/T=0.5$. At the middle of the upstroke the boundary layer again attaches as observed in all cases. One difference between the SD7003 and flat plate cases in combined pitch-plunge is that the LEV forms $\sim 0.25T$ earlier and persists longer in flat plate case. The stronger and durable LEV also increases the aerodynamic forces. The lift coefficient is in the range of $[0.25, 2]$ for flat plate case which is larger than the lift coefficient range of SD7003 airfoil.

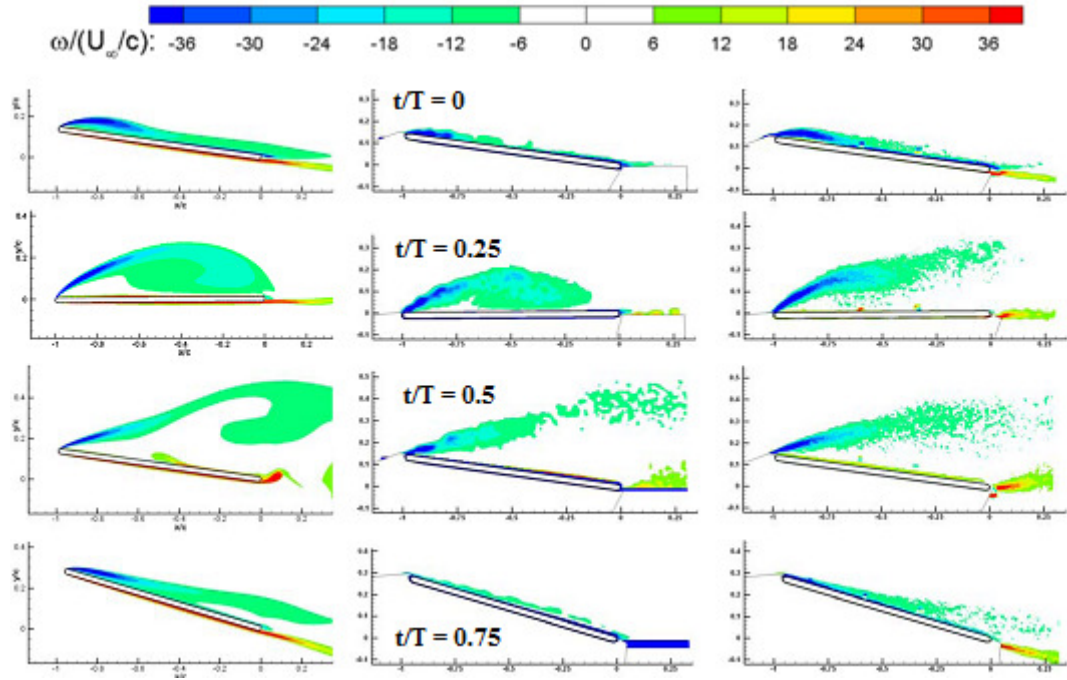


Figure 4.8 Normalized out-of-plane component of vorticity contours from present computation (left column), PIV experiment of University of Michigan [22] (middle column) and PIV experiment of AFRL [22] (right column) for combined pitch-plunge, $Re=60000$ $k=0.25$.

The pure plunge motion at $Re=60000$ and $k=0.25$ is also studied with the flat plate. Figure 4.9 shows the normalized vorticity contour results of present study (left column), URANS computations (middle column) and PIV experiment (right column) of University of Michigan (UM). At the beginning of motion the boundary layer seems attached and onset of LEV formation is not observed opposed to the pitch-plunge motion. The general vortex field is qualitatively similar with the SD7003 case in all results. On the other hand, the durable and stronger LEV formation characteristic of flat plate is also observed in pure plunge motion. The CW LEV formation at $t/T=0.25$ could be observed in all results. Also the TEV separates more quickly in flat plate cases. The formation of TEV could be seen at $t/T=0.333$ and it separates before $t/T=0.417$. The CCW rotating vortex on the suction side is first seen at $t/T=0.25$ and diffuses until $t/T=0.417$. The vortex core moves with velocity of approximately $1.8 c/T$ as could be seen in Figure 4.9. This vortex is also observed in

SD7003 cases but here it is somewhat larger. The consistency between all results for both cases could be sourced from not having pressure gradient due to the model geometry itself. More complex geometries introduce difficulties in terms of grid generation, solution procedures and modeling.

Pitch-plunge and pure plunge motions have mean lift coefficients of 0.774 and 0.759, and mean drag coefficients of 0.061 and 0.162 respectively. By decreasing the strength of LEV combining pitch motion to the plunge enhances the aerodynamic force characteristics for flat plate. This is the same result found for SD7003 cases.

Figure 4.10 and 4.11 shows the lift and drag time histories for flat plate cases respectively. The present solutions agree well with 3D LES solutions in pure plunge motion as in SD7003 case. However for pitch-plunge motion (Figure 4.11) present solution (blue) shows a greater increase in the lift peak amplitude. It is convenient to note that there are not any experimental or high fidelity LES solutions for this case. The red line is the result of 3D LES solutions for SD7003 case and plotted here again to have a conclusion about the effect of geometry. It could be seen that in Figure 4.11 the present solution (blue) agrees well with the other URANS solution (green) in this case in terms of lift coefficient history. On the other hand in drag coefficient history during the upstroke (Figure 4.11) the two URANS solutions shows difference which is not observed in pure plunge case (Figure 4.10).

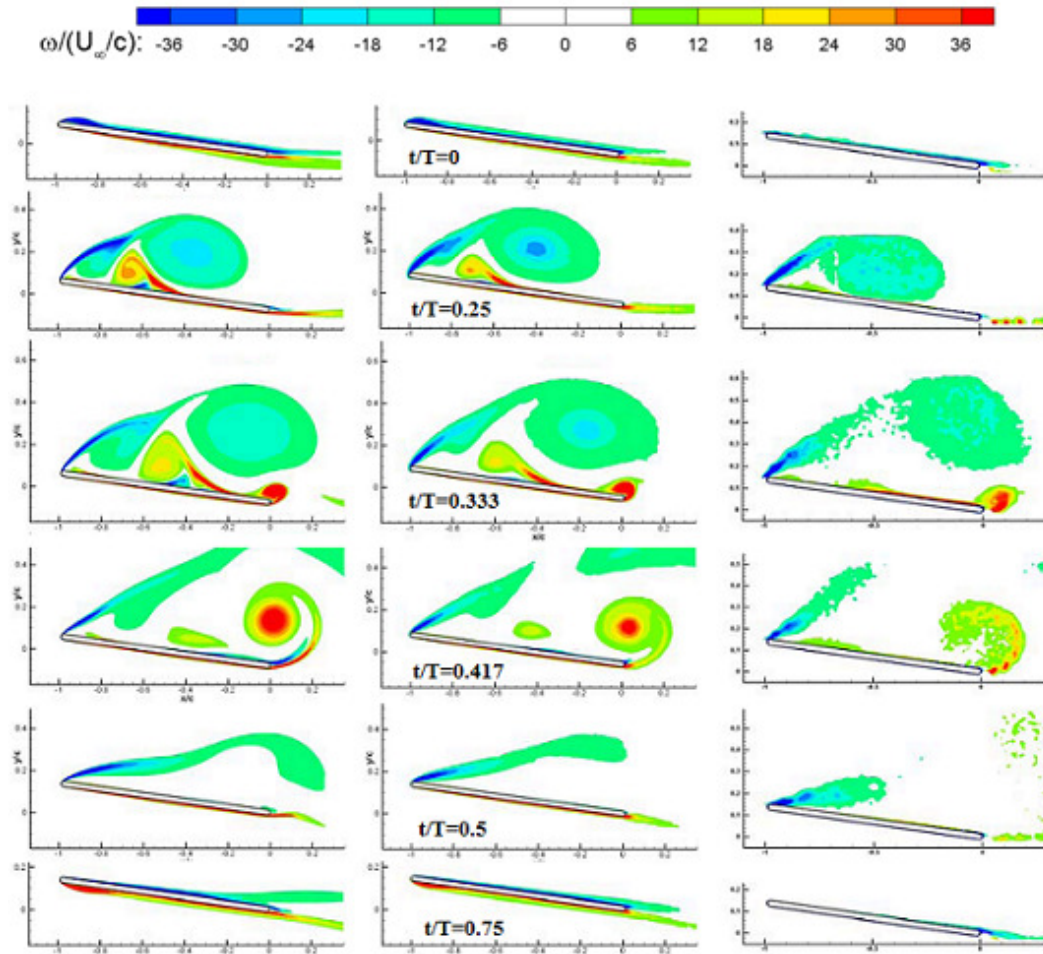


Figure 4.9 Normalized out-of-plane component of vorticity contours from present computation (left column), URANS computations of Uni. of Michigan [22] (middle column) and PIV experiments of Uni. Of Michigan [22] (right column) for pure plunge, $Re=60,000$ at $k=0.25$.

The present study catches a LEV generation in pitch-plunge case of SD7003 airfoil and that lead us to have difference with other results in terms of the amplitude of the lift peak (Figure 4.7). This behavior is not observed for flat plate case with same Reynolds number and reduced frequency. In flat plate case, the rounded edges force the airfoil towards transition and also the strength of the LEV increases. As one could conclude that the present method predicts the flowfield better for deep dynamic stall cases.

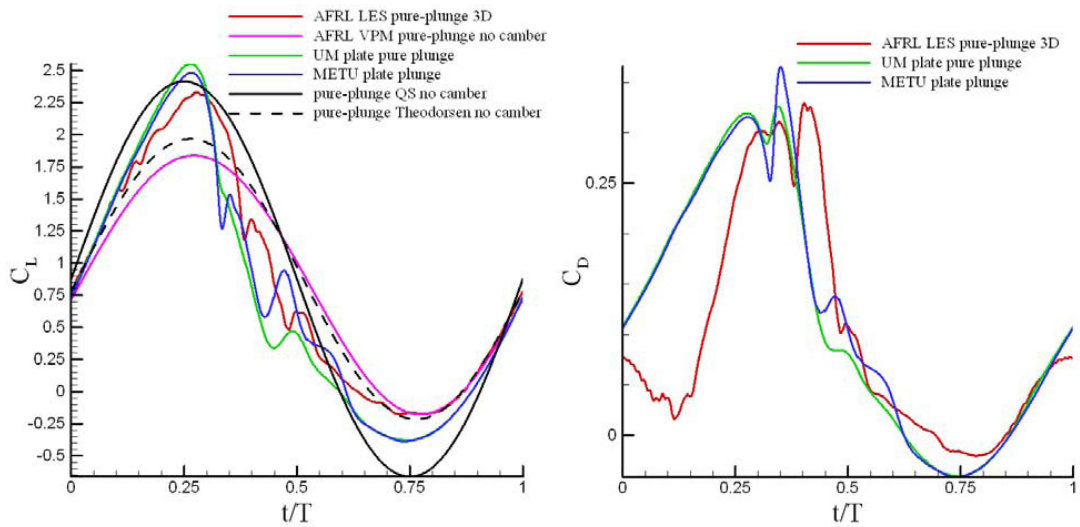


Figure 4.10 Lift coefficient history (left) and drag coefficient history (right) for pure plunge motion of a flat plate at $Re= 60000$ and $k=0.25$ [22].

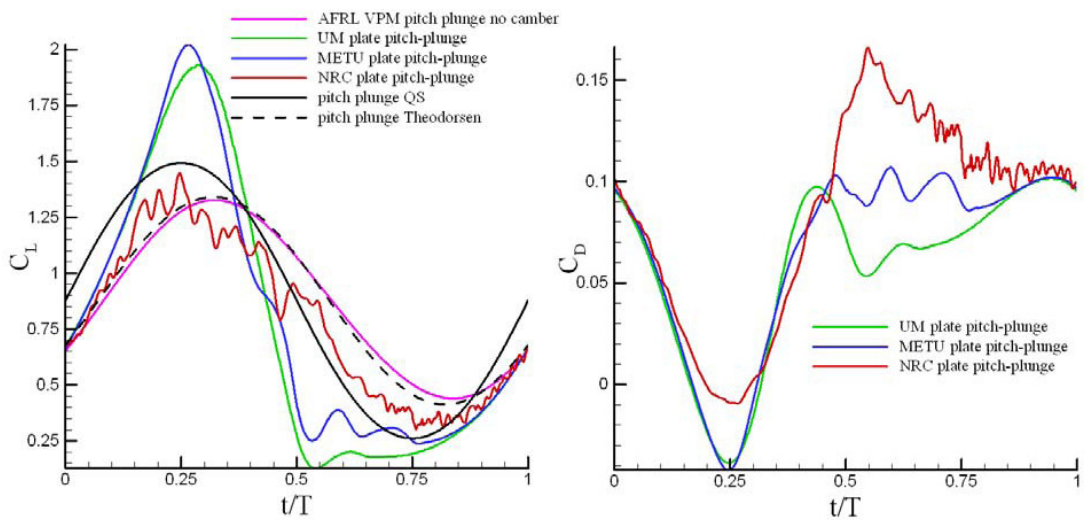


Figure 4.11 Lift coefficient history (left) and drag coefficient history (right) for combined pitch-plunge motion of a flat plate at $Re= 60000$ and $k=0.25$ [22].

4.5 Effect of Reduced Frequency

The baseline motion also studied for high frequency and low plunging amplitude. The reduced frequency is chosen as $k=3.93$ and the plunging amplitude is taken as $h_0=0.05$ ($St=0.125$). The mean angle of attack is taken as $\alpha_0=4^\circ$. These motions are more aggressive than the baseline motion and similar to the dynamic stall of helicopter blades. Figure 4.12 shows the time histories of angle of attack during high reduced frequency cases. Different that low frequency cases both pitch-plunge and pure plunge motions have same effective angle of attack history only with a $0.1T$ lag.

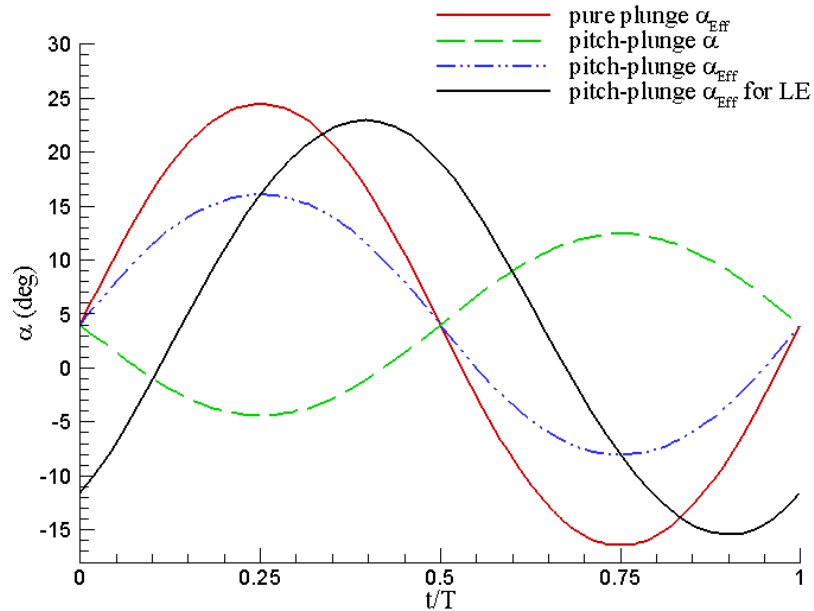


Figure 4.12 Time histories of geometric and effective angle of attack over one period of pure plunge and combined pitch-plunge motions at $Re=60000$, $k=3.93$ and $h_0=0.05$.

The pure plunge motion is studied at $Re=60000$ and $k=3.93$ and compared with experimental results available in literature [61]. Figure 4.13 and 4.14 show the velocity and vorticity contours for that motion respectively. The experimental results are again taken from PIV experiments of AFRL but not related with AVT-149. At that reduced frequency and low plunging amplitude the flow is likely attached over

the whole period and a small LEV formation is observed. The LEV forms at the end of downstroke ($t/T=0.5$) which could be seen at Figure 4.14. The vortex moves towards the trailing edge with a velocity of approximately $0.2 c/T$. At the beginning of motion a CCW TEV is observed which detaches from the airfoil surface very quickly and leaving its place to a CW TEV formation at $t/T=0.25$. This vortex grows until $t/T=0.75$ and detaches from the airfoil surface. A reversed Karman vortex street, which generates positive thrust over whole period, is obtained from the detached vortex structures in the wake of the airfoil. In all phases of motion the vortices are identifiable by the separated high velocity regions. These regions could be observed at $t/T=0.5$ at four locations ($0.05c$, $0.25c$, $0.75c$ and $0.95c$).

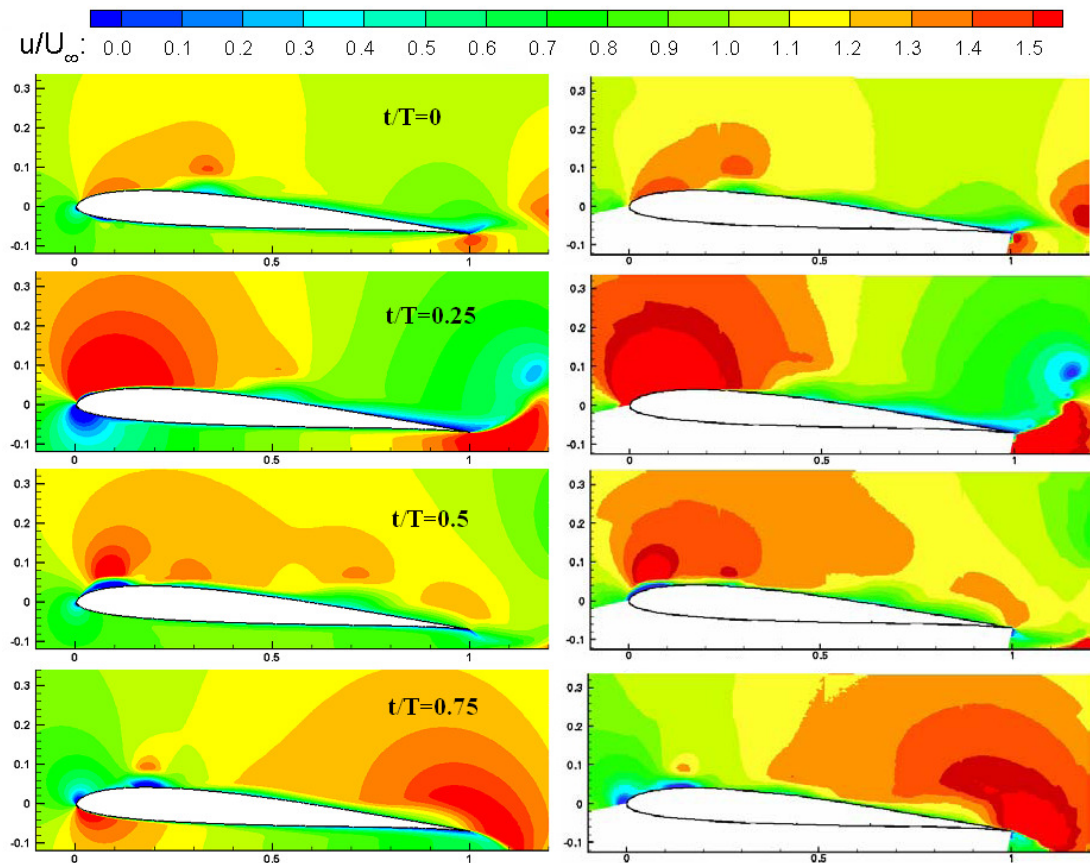


Figure 4.13 Contours of normalized u-velocity for pure-plunge, computational (left column) and experimental results from [61] (right column) at $Re=60000$, $k=3.93$ and $h_0=0.05$.

Figure 4.15 shows the normalized vorticity contours for combined pitch-plunge motion of SD7003 airfoil at $Re=60000$ and $k=3.93$. In this case no LEV formation is observed. Only two consequent reverse rotating trailing edge vortices are observed. The CCW TEV detaches from airfoil surface at $t/T=0.25$ and the CW TEV detaches at $t/T=0.75$. The lack of LEVs shows that for high reduced frequency cases even the inviscid methods and analytical methods could give accurate results for high frequency cases. Again in this motion we observe a reverse Karman vortex street but this time shedding is two times greater so two crests are observed in drag time history.

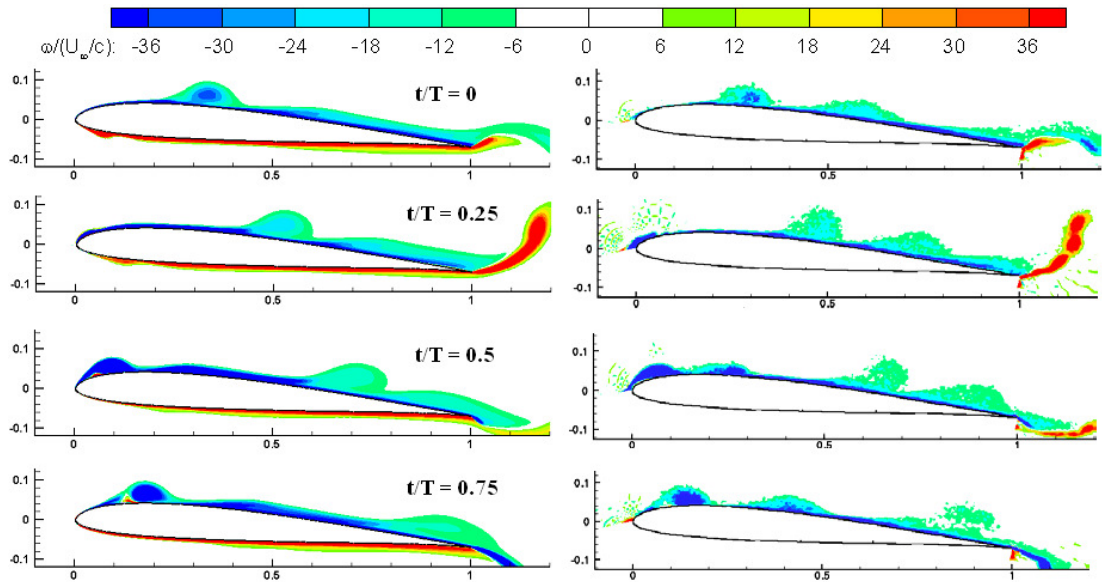


Figure 4.14 Contours of normalized vorticity from present computation (left column), experimental results from [61] (right column) at $Re=60000$, $k=3.93$ and $h_0=0.05$.

The effective angle of attack history for high frequency cases is given in Figure 4.12. The pivot effect results having a shift in high frequency cases with the baseline cases (Figure 4.1). This study also reveals the dominant reference point in terms of defining the effective angle of attack, leading edge or the rotating center. In low frequency cases effective angle of attack histories for pure plunge and pitch-plunge

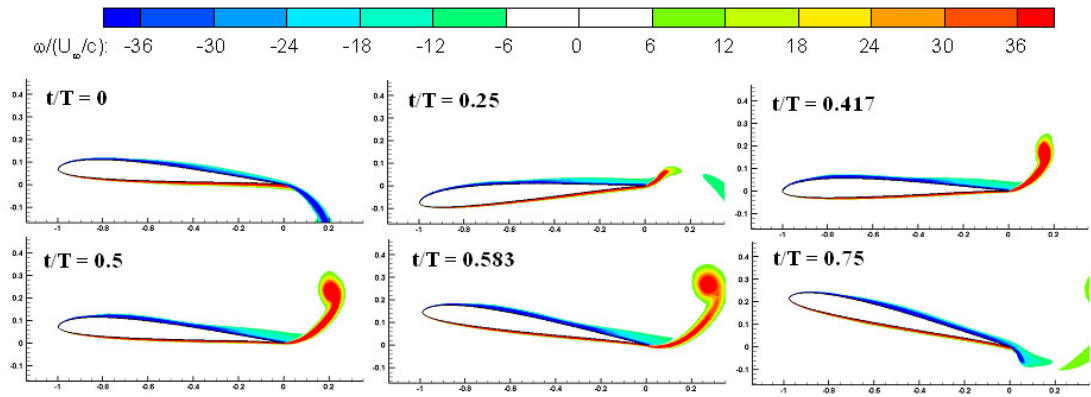


Figure 4.15 Normalized vorticity contours for combined pitch-plunge at $Re=60000$, $k=3.93$ and $h_0=0.05$.

motions are in the same sine form just differing in terms of amplitudes. On the other hand, in high frequency cases there exists a shift in effective angle of attack histories that includes pivot effect. As could be seen in Figure 4.16 the lift histories are also have a shift and that result encourages one to comment on that the pivot effect is the driving force on aerodynamic force generations. Moreover in those cases the lift time histories are periodic and the main mechanisms in aerodynamic force generation is the non-circulatory loads. The combined pitch-plunge motion has two crests in drag time history at $t/T=0.25$ and $t/T=0.75$. As could be seen in Figure 4.15 the CCW TEV moves towards up and the CW TV moves to the bottom of the centerline in the wake region. This is the general characteristic of thrust indicative vortex street, known as reverse Karman vortex street. The vortices are inducing momentum surplus in the wake region. The mean lift coefficients are 0.838:0.703 and drag coefficients are -0.2677:-0.0664 for pitch-plunge and pure plunge motions respectively. As a result it seems that combining pitching motion have enhanced the force characteristics of plunging airfoil. This is the same result with baseline motions. As a future work the relation of different combinations of motions could be studied in terms of responsible mechanisms and force characteristics.

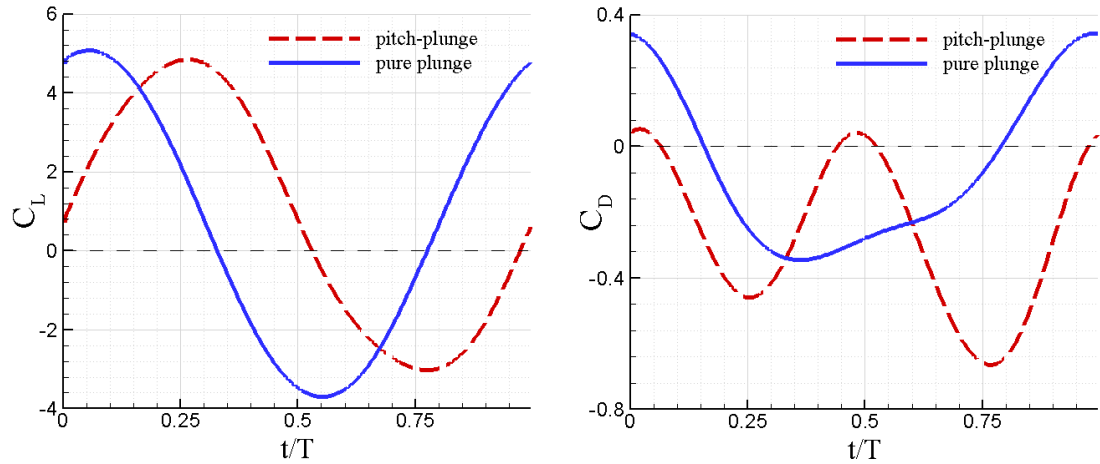


Figure 4.16 Time histories of lift coefficients (left) and drag coefficients (right) for high frequency cases at $Re=60000$, $k=0.25$ and $h_0=0.05$.

4.6 Effect of Reynolds Number

The baseline motions are also studied for three different Reynolds numbers to investigate the Reynolds number effect on aerodynamic force generation. Figure 4.17 and 4.18 show the lift and drag time histories for pitch-plunge and pure plunge motions respectively at low reduced frequency. The pure plunge seems independent of Reynolds number in terms of aerodynamic forces. On the other hand a time shift is observed in the peak value of lift for combined pitch-plunge motion. Moreover that time shift shows itself as a drop in the amplitude of minimum drag value at $t/T=0.25$ (Figure 4.18). The aerodynamic forces are following similar sinusoidal trend with altering Reynolds number for both motions. On the other hand the LEV forms at an earlier phase of the motion and stays for a shorter time on the airfoil for decreasing Reynolds number. The forming time of LEV could be observed by the width of the positive value for lift. That loss in the width shows itself as a drop in the mean lift coefficient. The mean lift coefficients for combined pitch-plunge motion are 0.683, 0.802 and 0.856 at Reynolds numbers of 10000, 30000 and 60000 respectively. Figure 4.18 shows that decreasing Reynolds number also flattens the drag coefficient time history in combined pitch-plunge motion. Therefore there exists a narrower range for negative values of drag coefficient. As expected the mean drag coefficient

increases with decreasing Reynolds numbers for combined pitch-plunge motion. The mean drag coefficients for that motion are 0.0609, 0.0376 and 0.0224 at Reynolds numbers of 10000, 30000 and 60000. As a result it seems that the massive separation case is particularly insensitive to the Reynolds number whereas the shallow dynamic stall case which has moderate angle of attack history is sensitive to the Reynolds number.

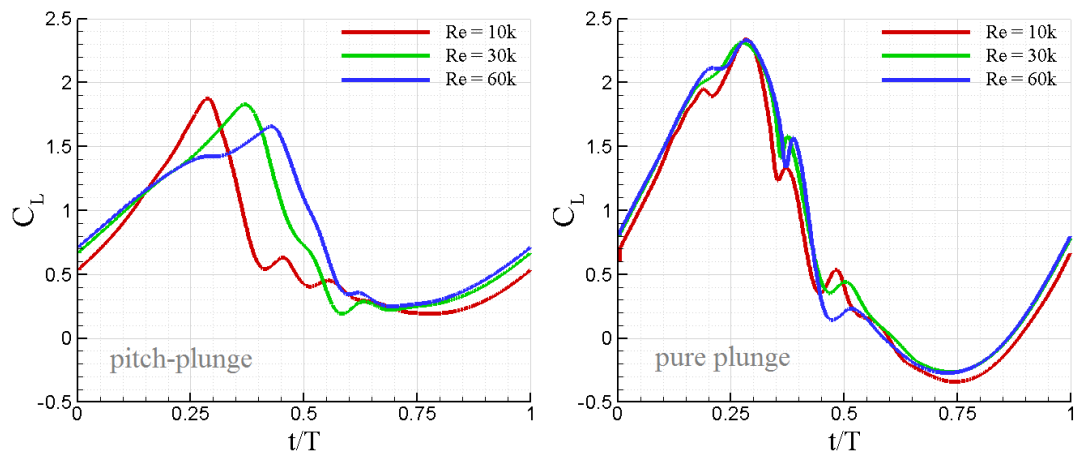


Figure 4.17 Time histories of lift coefficients for pitch-plunge (left) and pure plunge (right) at three different Reynolds numbers.

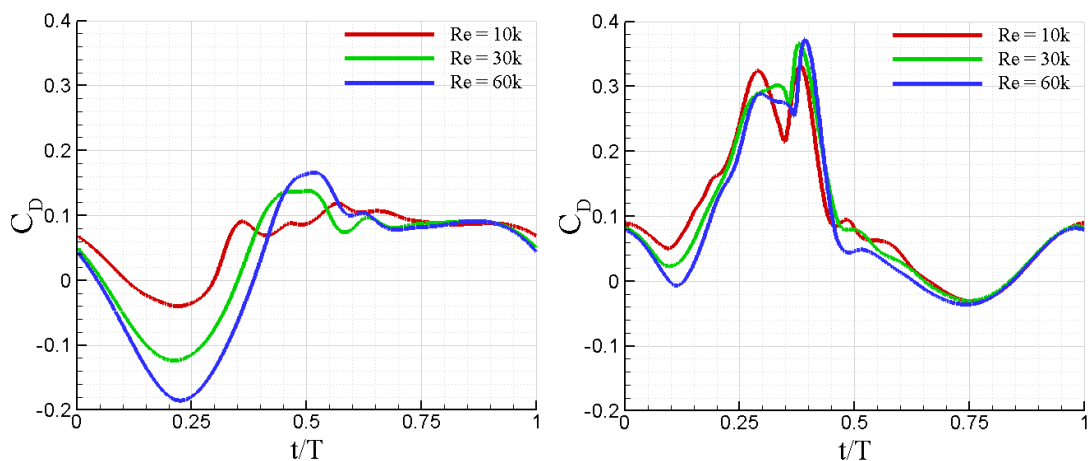


Figure 4.18 Time histories of drag coefficients for pitch-plunge (left) and pure plunge (right) at three different Reynolds numbers.

The only difference in force coefficients are observed for combined pitch-plunge motions. Thus the normalized vorticity contours of this motion for different Reynolds numbers are visualized in Figure 4.19. It could be seen that in lift coefficient history with decreasing Reynolds number the formation of the LEV is quicker during the downstroke. Moreover this LEV separation attaches quickly and the width of the positive lift curve is narrower. The time instants $t/T=0.25$, 0.333 and 0.417 are nearly the peak locations of cases $Re=10000$, 30000 and 60000 . The similar vortex structures could be observed for this diagonal fashion in Figure 4.19.

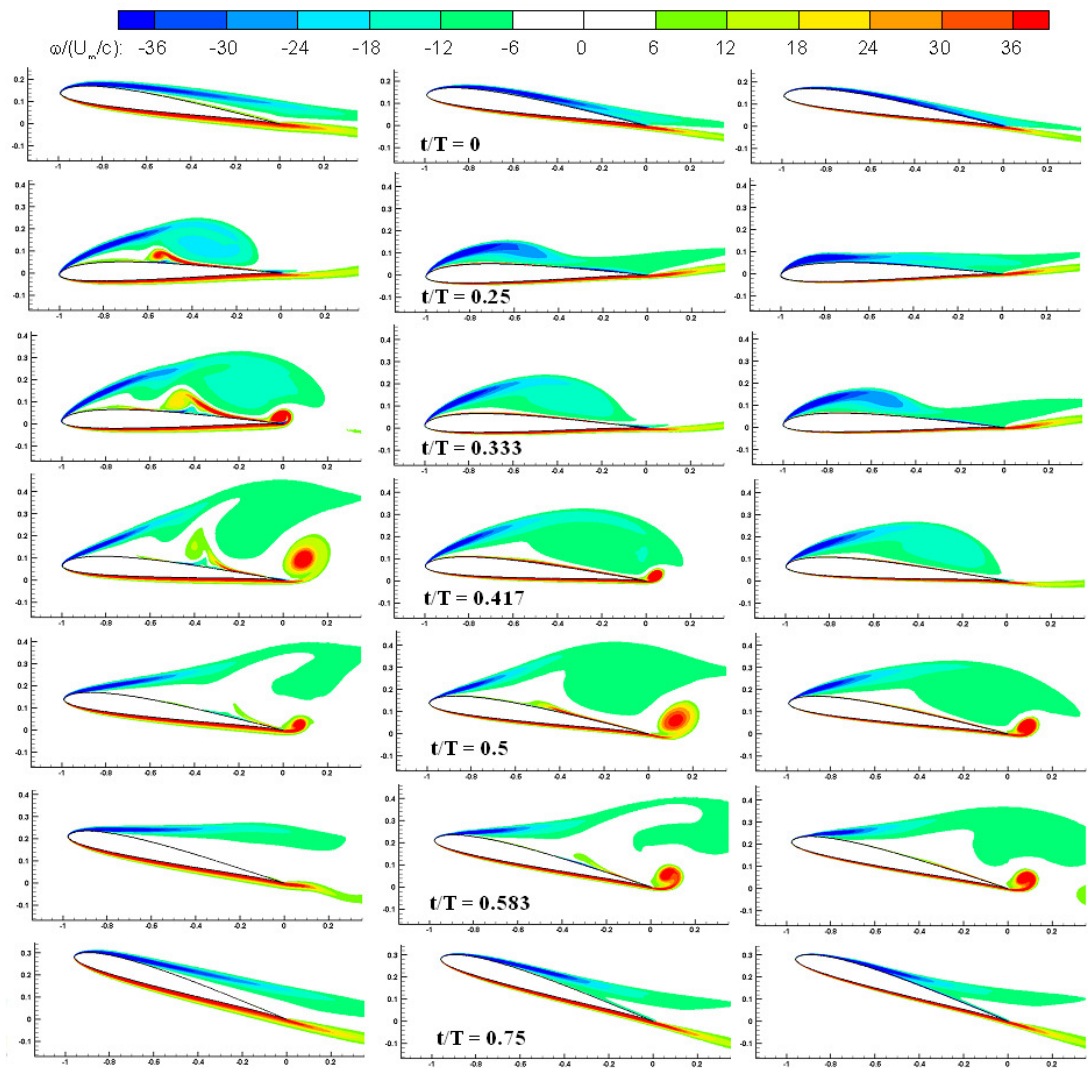


Figure 4.19 Contours of normalized vorticity for combined pitch-plunge motion at $Re=10000$ (left column), $Re=30000$ (middle column) and $Re=60000$ (right column), $k=0.25$

The diagonal view for different Reynolds numbers (compare $t/T=0.25$ for $Re=10000$, $t/T=0.333$ for $Re=30000$ and $t/T=0.417$ for $Re=60000$) also show the LEV formation delay with altering Reynolds number.

On the other hand comparing the vortex fields at same time instant could show the same delay phenomenon. At the beginning of the motion ($t/T=0$) the boundary layer tends to separate at $Re=10000$ whereas at other Reynolds numbers the boundary layers seem to be totally attached. After this instant, at $t/T=0.25$ the LEV is at the back half of the chord at $Re=10000$ whereas the onset of LEV formation is observed at $Re=30000$. For the same instant the boundary layer seems attached at $Re=60000$. These differences during the downstroke lose their effects in the upstroke which is a kind of passive phase of the motion.

CHAPTER V

HOVERING RESULTS

This chapter is devoted to the results of flapping airfoils in hover. The hovering motions consist of horizontal and vertical translations and pitching motion around the quarter chord without any free-stream velocity. The combination of all these motions results that the pivot point traces a figure-of-eight in hover. The effects of two important similarity parameters, Reynolds number and reduced frequency, are investigated. The instantaneous vorticity fields and the aerodynamics forces are visualized and the force generating mechanisms are discussed.

6.1 Hovering Kinematics

Different figure-of-eight motions of SD7003 airfoil are studied for hovering cases. The motion is defined by Lissajous curves which are given by Equations 3.11 to 3.13. The parameters in those equations are defined in section 3.6. The amplitude of vertical translation is studied for seven different values as 0, 0.25, 0.5, 0.75, 1, 1.25 and 1.5 at $Re=1000$. The reduced frequency is defined as the half of the vertical translation amplitude for figure-of-eight motions as given by Equation 3.17. Moreover the effect of Reynolds number is investigated for $Y=0.5$ case for eleven different values from 500 to 5500. The capability of the code for ultra low-Reynolds number flows has been shown in Reference [62] by comparing the numerical results with experimental results.

6.2 Effect of Vertical Translation

The positions of airfoil during figure-of-eight motion are given in Figure 5.1. The horizontal translation and angular variation definitions are same for all cases studied in hover mode. Thus only the vertical position of airfoil differs for each case. The denoted case in Figure 5.1 is for the $Y=0.5$ case. This case is also studied to investigate the Reynolds number effect. Figure 5.2 shows the flapping paths of hovering airfoil for different vertical translations, 0 to 1.5. At each time instant, the horizontal location and geometric angle of attack of the airfoils are the same, only the

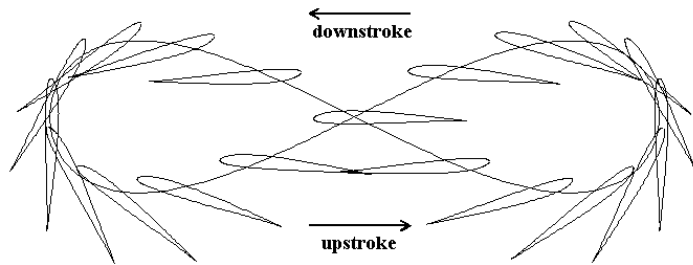


Figure 5.1 Sample figure-of-eight motion for $Y=0.5$. Positions of airfoils each with $0.05T$ time interval.

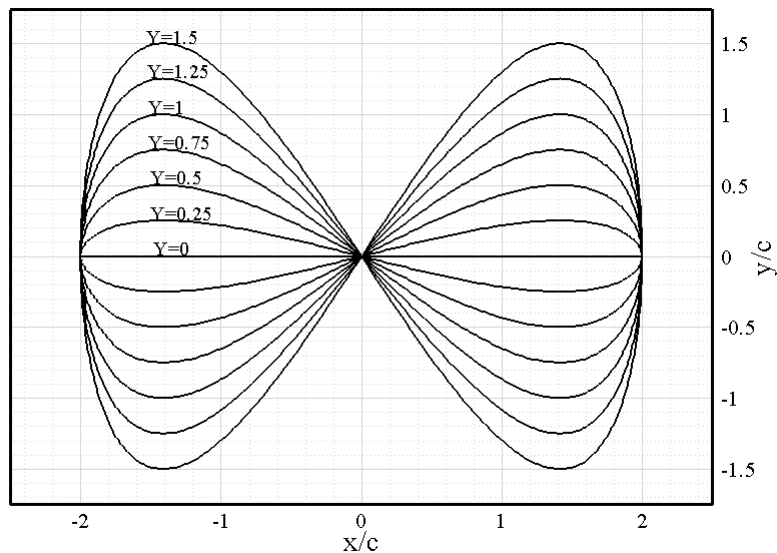


Figure 5.2 Flapping paths of hovering airfoil with different vertical translation amplitudes.

vertical locations differ. The vertical translations larger than $Y=0.5$ seem unfeasible for insect or bird flight but these values will help to clarify the behavior of the investigated parameter at extremes. The $Y=0$ case is the normal hover case that is defined by Freymuth [40]. Due to the experimental difficulties hovering literature mostly based on cases with two degree of freedom motions. The vertical translation is considered recently in literature [63]. In order to enhance the study a wide range of parameters are investigated throughout the thesis.

Figure 5.3 shows the normalized vorticity contour of normal hovering motion with vertical translation amplitude of $Y=0$. The suction side of the SD7003 airfoil is cambered whereas the pressure side is flatter. During the upstroke the pressure side turns out to be the upper surface and this will help us to observe the effect of surface geometry and asymmetric airfoil effect. In all cases due to the asymmetry of the airfoil, slight differences in vortex structures and time delay in formation of vortices are expected between upstroke and downstroke. In all figure-of-eight motions, different than the $Y=0$ case, the vortices are more diffusive during upstroke. During the $Y=0$ case, the vortex structures seem to be similar but in lift time history (Figure 5.6) a slight drop is observed during upstroke. At $Y=0$ case there is no vertical velocity and the main effect on LEV formation is the sudden change of angle of attack due to the rotation. The LEV that could be observed at the beginning of the downstroke is formed during the last quarter ($t/T \sim 0.75$) of the previous period. The curved shaped TEV squeezes the flow on the upper side of the airfoil and generates a secondary vortex-like structure at the wake of LEV ($t/T=0.0$ in Fig. 5.3). In other cases, the LEV forms earlier and that secondary structure is not observed (Fig. 5.4 and 5.5). The existence of vertical velocity forces the massive separation and LEV formation to occur at an earlier instant.

Figures 5.6 and 5.7 show lift and drag coefficient histories of hovering motion for seven different vertical translation amplitudes. In order to compare the quantities clearly, the results are represented in two figures for each force coefficient. The vortex structures are the only sources of variations in these force coefficients and it will be more elucidative to explain the generation of forces in terms of vortex

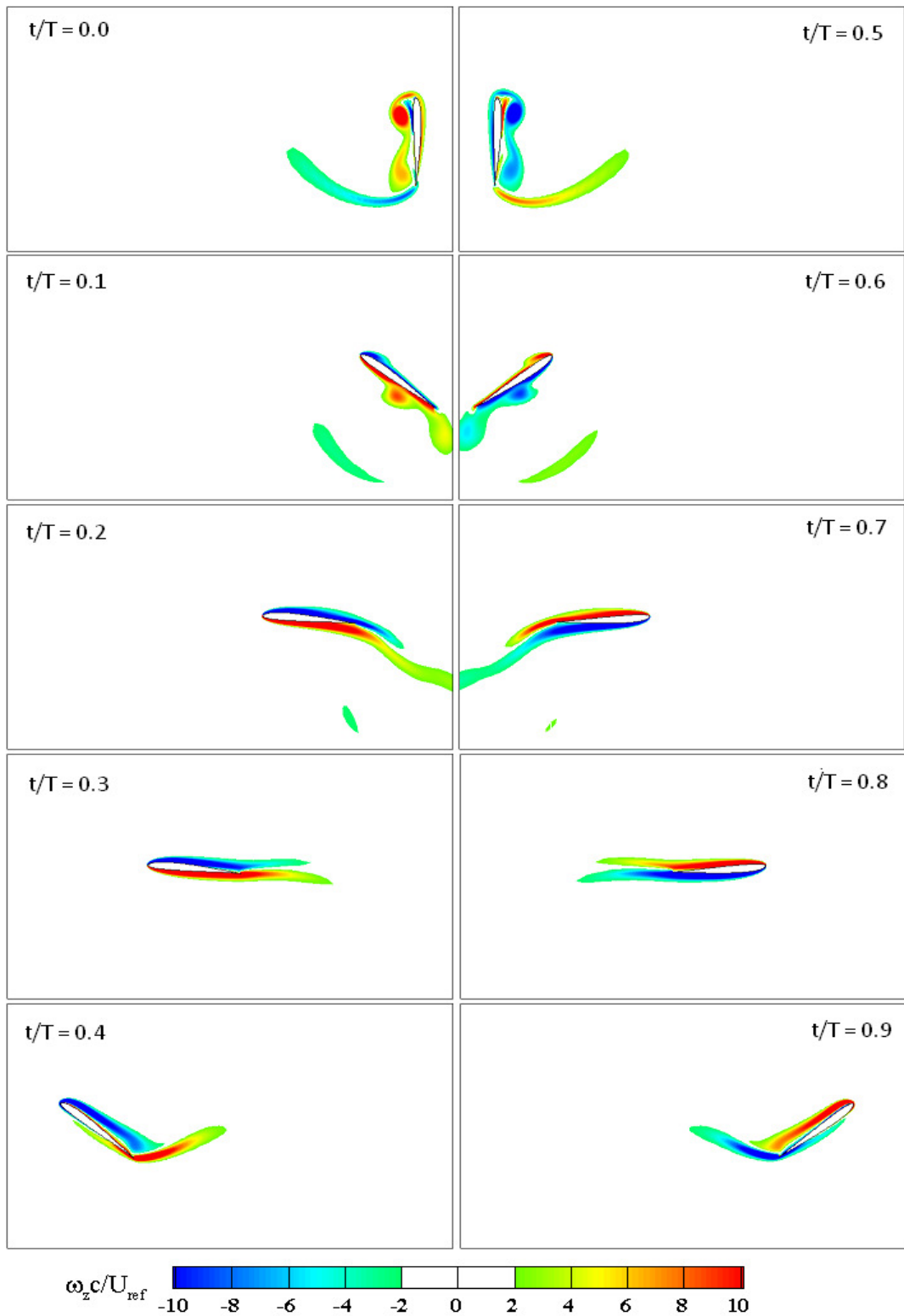


Figure 5.3 Normalized vorticity contours of $Y=0$ hovering at $Re=1000$. Red regions denote positive vorticity (CCW swirling) and blue regions denote negative vorticity (CW swirling).

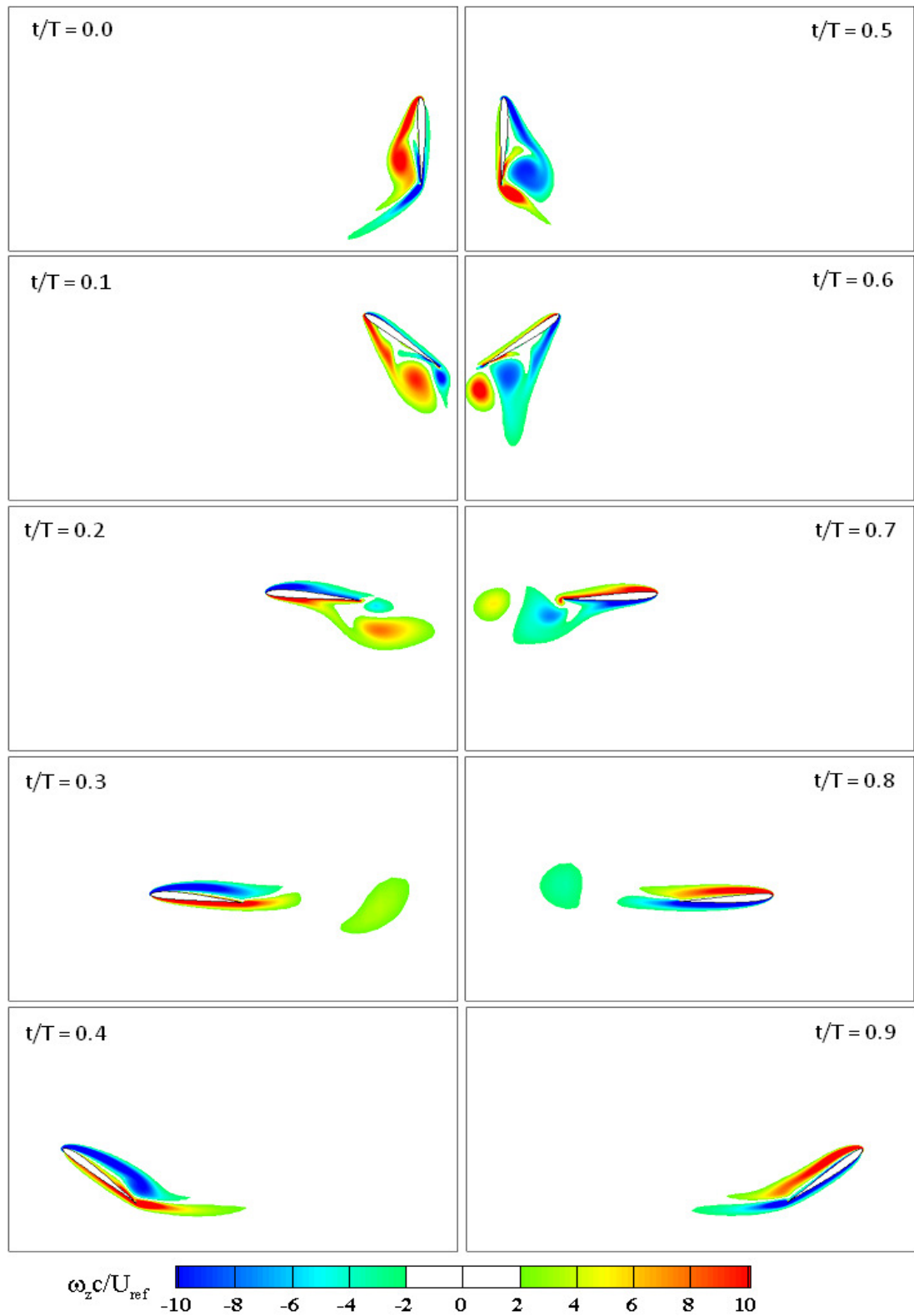


Figure 5.4 Normalized vorticity contours of Y=0.5 hovering at Re=1000. Red regions denote positive vorticity (CCW swirling) and blue regions denote negative vorticity (CW swirling).

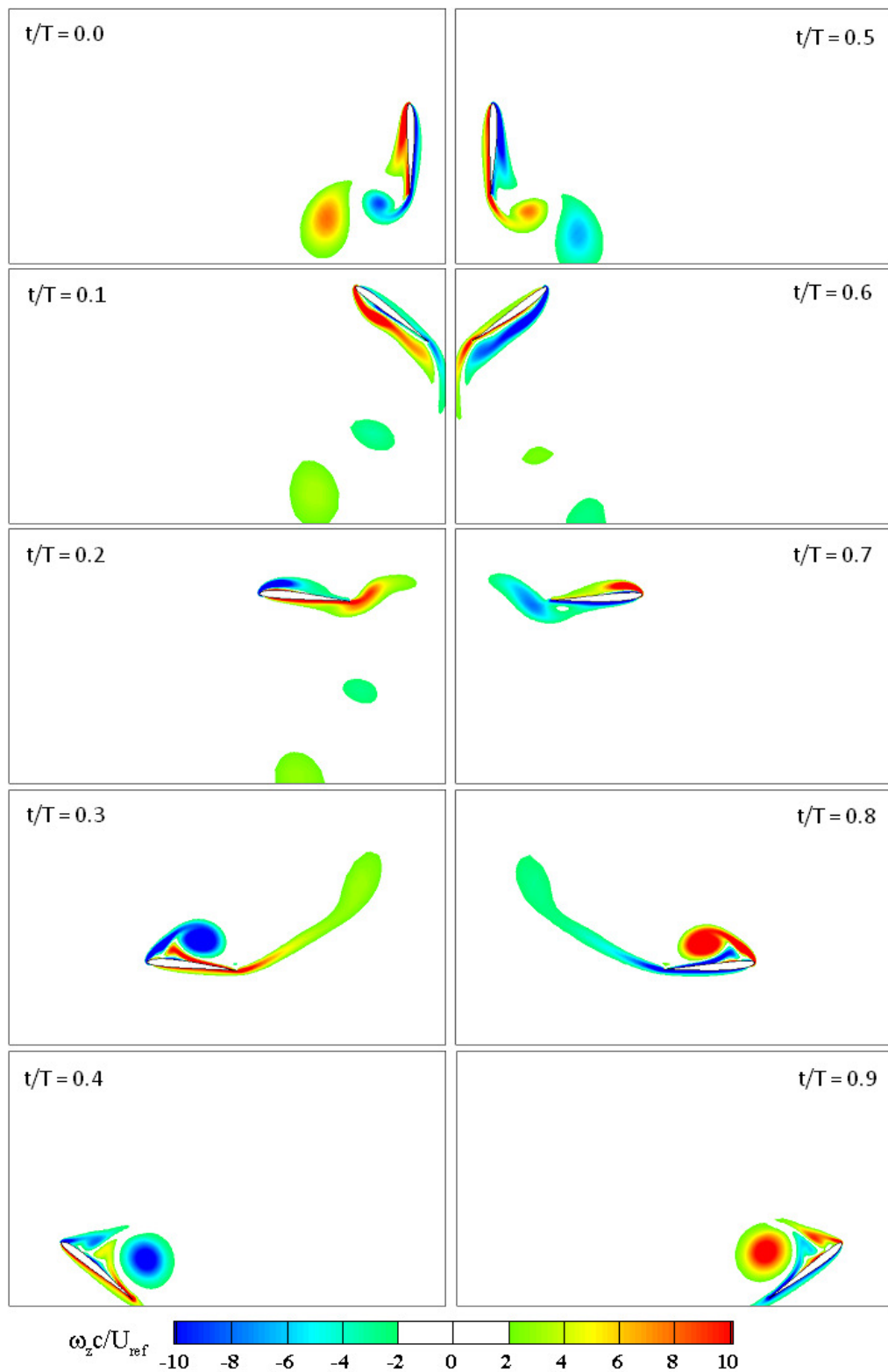


Figure 5.5 Normalized vorticity contours of Y=1 hovering at Re=1000. Red regions denote positive vorticity (CCW swirling) and blue regions denote negative vorticity (CW swirling).

structures. The one significant distinction of $Y=0$ case is that the LEV hits to the airfoil surface whereas in all other motions airfoil escape from the LEVs. The LEV on the airfoil creates a low-pressure region on the pressure side of the airfoil until it detaches. The significant lift drop until $t/T \sim 0.15$ is the effect of that low pressure region (Figure 5.6). After that instant the new LEV starts to form and the lift coefficient reaches its peak at $t/T \sim 0.4$. The same process occurs for the upstroke again but this time in reverse direction. Also during the whole upstroke up to $t/T \sim 0.3$ drop in lift coefficient is observed whereas the drag coefficient is totally similar for both strokes. Between the two strokes, the upper and lower surfaces of the airfoil change their roles and this is the reason for the lift drop in all cases. In all motions the chord of airfoil is vertical at the beginning of strokes ($t/T \sim 0.0$ and $t/T \sim 0.5$) so the vertical force coefficient is close to zero at those instants. On the other hand at those instants the horizontal forces have their maximum value as could be seen in Figure 5.7 for $t/T=0$ and $t/T=0.5$.

There are two different characteristics in lift coefficient histories. For the vertical translation amplitudes up to $Y=0.75$, the width of the cambered positive lift force curve is increasing whereas for vertical translation amplitudes greater than $Y=0.75$ that width is decreasing and a new deep in lift coefficient history starts to form at $t/T \sim 0.35$. Due to the high vertical velocity, one more LEV is generated at the end of downstroke between $t/T=0.4$ and $t/T=0.5$ and similarly at the end of upstroke between $t/T=0.9$ and $t/T=1$. This second LEV could be observed in Figure 5.5 at $t/T=0.4$ and $t/T=0.9$ as detaching from the airfoil surface. It is also observed that the detachment of the LEV results as a shift in the lift peaks towards the middle of the strokes with the increase of vertical translation amplitudes. It is also found that as the vertical translation amplitudes are increasing only the amplitudes of the force peaks and deeps increases, the general vortex fields are not altered after a point.

Figure 5.4 and 5.5 are the normalized vorticity contours of two figure-of-eight motions with $Y=0.5$ and $Y=1$, respectively. In neither of these cases, LEV hits the airfoil surface. Thus the airfoils are free from the suction regions produced by the vortices. In $Y=0$ case, a secondary vortex structure due to the squeezing of the TEV

is observed at the beginning of motion (Figure 5.3, $t/T=0.0$). For $Y=0.5$ case, due to the vertical velocity of the airfoil the LEV is free from the TEV and easily detaches from the airfoil surface (Figure 5.4, $t/T=0.0$). For this case the growing time of the LEV is larger and this results a gentle slope in lift coefficient for $Y=0.5$. The LEV starts to form at $t/T=0.85$ in previous stroke and detaches from the airfoil surface at the beginning of present period. The asymmetry of the airfoil shows its effect on the vortex field for figure-of-eight motions more aggressive than $Y=0$ case. Also comparing the vortex structures during the downstroke with their counterparts during the upstroke shows the effect of airfoil geometry on figure-of-eight motion. The vortices generated with the effect of relatively flatter geometry during the upstroke are weaker and more diffusive. This could also be observed as a drop in lift coefficient as stated before.

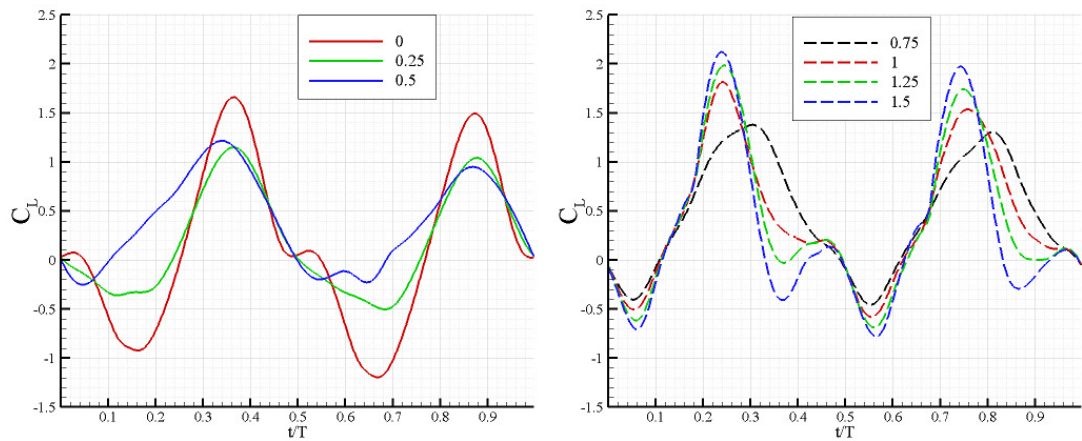


Figure 5.6 Time histories of lift coefficients for hovering motions with different vertical translation amplitudes at $Re=1000$.

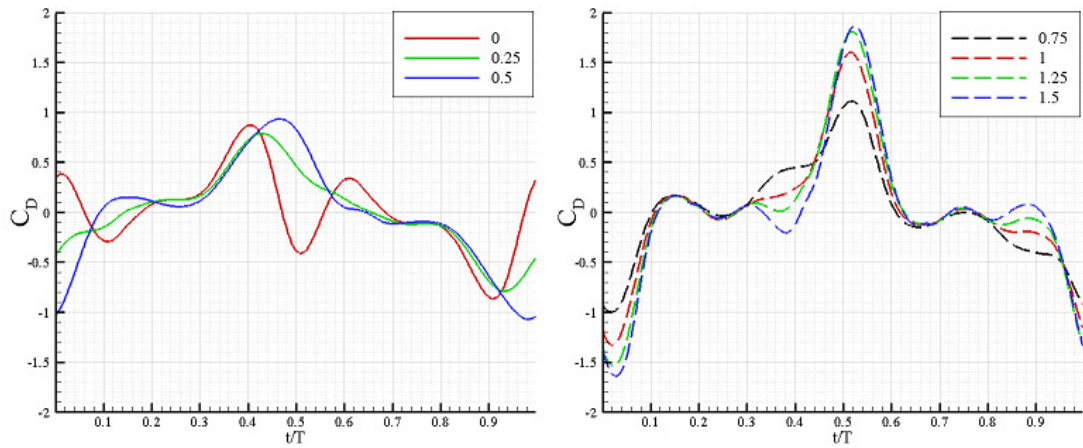


Figure 5.7 Time histories of drag coefficients for hovering motions with different vertical translation amplitudes at $Re=1000$.

The $Y=1$ case shows similar characteristics with the $Y=1.25$ and 1.5 cases. The only difference between these cases is the strength of the vortices which results to increase the amplitude of deeps and peaks in the force histories. Even the formation durations of the vortices are same for these motions. At the beginning of $Y=1$ hovering motion ($t/T=0.0$), two vortex structures are observed. The LEV is generated during the previous period at $t/T=0.7$ due to the translation while the TEV starts to form at the end of previous period due to the rotation of the airfoil. The LEV appears in the field of interest at about $0.4T$ time. This again shows that the vortices become stronger with increasing vertical translation amplitude. At $t/T=0.1$ a new TEV starts to form and after $0.1T$ time that TEV detaches from the airfoil surface. The trace of this TEV could be observed at $t/T=0.3$ which is not the case for $Y=0.5$ case. Moreover, at $t/T=0.1$ a LEV starts to form and that vortex separates between $t/T=0.2$ and $t/T=0.3$. The $Y=1.0$ case is the only case in which LEV forms in the middle of the stroke.

After the vertical translation amplitude exceeds $Y=1.0$ a secondary deep at the end of the stroke is observed at $t/T=0.4$. Figure 5.8 shows the pressure coefficient contours for $Y=1$, 1.25 and 1.5 cases with the instantaneous streamlines. In all cases, the former LEV generates a suction region on the airfoil that causes the increase of lift. On the other hand, for $Y=1.5$ case a vortex is generated on the lower surface of the

airfoil. Due to that vortex, the pressure on the lower surface is also decreasing and the secondary lift deep occurs. It is also observed that with increasing velocity, the LEV core is pushed upwards. Thus the generated suction region does not affect the pressure distribution on the airfoil that much. For $Y=1.0$ another strong LEV is observed on the upper surface of the airfoil with the detachment of the previous LEV. The vortex core of this LEV could be hardly seen in $Y=1.25$ case and the suction region is similar with $Y=1.0$ case. For $Y=1.5$ case, this vortex totally disappears and the suction region seems free from the effect of this LEV compared to the other two case. This secondary vortex is not a desired phenomenon for a hovering case due to the loss of lift. The same characteristic is also observed in downstroke as could be seen in Figure 5.6. As expected, the vortices are weaker in downstroke due to the flatter upper surface thus relatively a smaller loss in lift is observed. The drag coefficient increases during downstroke since the motion is in reverse direction (positive x-direction).

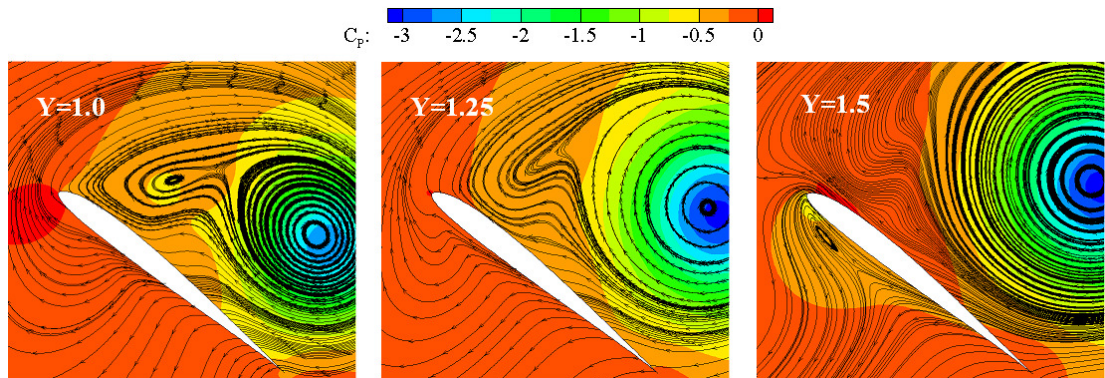


Figure 5.8 Pressure coefficient contours with streamlines for three different Y values at $t/T=0.4$, $Re=1000$.

The mean force coefficients for hovering motions with seven different vertical translation amplitudes are listed in Table 5.1. With increasing vertical translation amplitude mean lift coefficient is in a smooth increasing-decreasing trend. At the

moderate values of vertical translation amplitudes, mean lift coefficient has its local maximum value. The mean drag values are not following such a trend as lift.

It is obvious that with increasing vertical translation more energy must be supplied to the system. Thus, one must also consider this to compare the efficiency of motions with each other. In computations we ignored the mass of the airfoil and the power input to the system is considered as the work done on air by flapping motion. From momentum theory, the work done on air is the change of its kinetic energy per unit time which is given by equation 5.1.

$$P^* = \frac{1}{2}(\rho cl\bar{V})(2\bar{V})^2 = 2\rho cl\bar{V}^3 \quad (5.1)$$

$$\bar{V} = \frac{1}{T} \int_t^{t+T} (\dot{x}(t)^2 + \dot{y}(t)^2)^{3/2} dt \quad (5.2)$$

where c is airfoil chord, ρ is air density, l is span, T is period of motion, \bar{V} is the mean velocity over a period, $\dot{x}(t)$ and $\dot{y}(t)$ are horizontal and vertical velocities of the airfoil respectively. The power coefficient could be calculated as given in equation 5.3,

$$C_P = \frac{P^*}{\rho cl(\omega c)^3} = 2 \left(\frac{\bar{V}}{\omega c} \right)^3 \quad (5.3)$$

where ω is the angular frequency of the flapping motion. The aforementioned parameters let us to define a non dimensional power ratio for the figure-of-eight motion as given by equation 5.4,

$$\eta = \frac{\overline{C_L} V_{max}}{C_P} \quad (5.4)$$

where V_{max} is the maximum velocity over the period. This definition also makes the comparison of normal hovering with figure-of-eight hovering and different than the propulsive efficiency definitions in forward flapping flight. The defined efficiency is the ratio of the useful power to the power input to perform flapping motion.

Table 5.1 Mean lift and drag coefficients for different Y values at Re=1000

Y	0	0.25	0.5	0.75	1	1.25	1.5
C_L	0.124	0.188	0.382	0.473	0.431	0.382	0.312
C_D	0.010	0.011	-0.001	0.019	0.038	0.040	0.023

The efficiencies and mean lift coefficients for seven different vertical amplitudes are given in Figure 5.9. At the first look in Table 5.1, one can expect that Y=0.75 case is the optimum case among the studied seven case. However, power required for maintaining a figure-of-eight motion is proportional to the cube of the velocity and therefore, the power ratio in Ea.5.4 is strongly related with the vertical translation amplitude. By aforementioned efficiency definition, the Y=0.5 case is found to be the most efficient hovering motion. There are two interesting results in Figure 5.9 for the optimum case;

- The most efficient case has the smallest mean drag coefficient, which is one order of magnitude smaller compared to its counterparts,
- The most efficient case has the steepest ascent in terms of mean lift coefficient variation.

In forward flight of flapping airfoils the major aim is to have larger negative drag values during the period. On the other hand, in hover the drag force only cause

undesired oscillations in horizontal direction which will consume high energies. Moreover, in hover the major aim is to have higher lift coefficients to be capable of keep the air vehicle at fixed height with minimum energy.

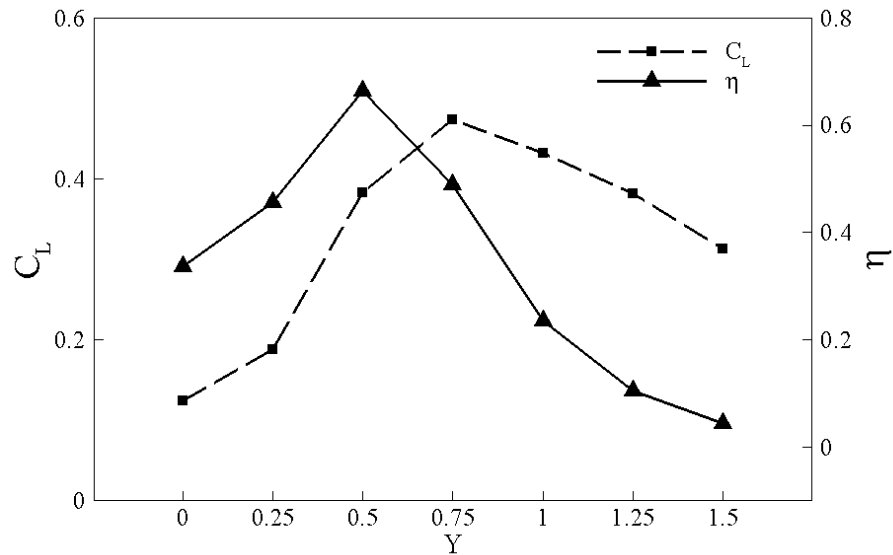


Figure 5.9 mean lift coefficients and efficiencies for investigated hovering motions.

The efficiencies and lift-to-drag (L/D) ratios for different hovering motions are tabulated in Table 5.2. It is also interesting to note that L/D is following the same trend with the efficiency for all vertical translation amplitudes except $Y=1.5$. The L/D ratio must be compared with the efficiency of the motion qualitatively since there is no direct relation between them for unsteady flapping motion. However, it is still a useful parameter especially if our points of interest are insects whose flapping frequencies could be as high as 250 Hz.

Table 5.2 Efficiencies and lift-to-drag ratios for different Y values at $Re=1000$

Y	0	0.25	0.5	0.75	1	1.25	1.5
η	0.34	0.46	0.66	0.49	0.24	0.10	0.04
L/D	12.6	17.4	272.5	25.3	11.3	9.5	13.4

6.3 Effect of Reynolds Number

The effect of Reynolds number on figure-of-eight type hovering is investigated by solving unsteady, laminar Navier-Stokes equations for eleven different Reynolds numbers ranging from 500 to 5500 with equal intervals. The $Y=0.5$ is found to be the optimum case among the seven different vertical translations in previous section, so it is chosen as the baseline motion for the following parametric study. All presented results in this section belong to $Y=0.5$ hovering.

Figure 5.9 shows the lift and drag coefficient histories of $Y=0.5$ hovering motion at five different Reynolds numbers. It is found that representing the results for five different Reynolds number is adequate to show the general trend. The $Re=1000$ is the result of previous section and the other results are represented for $Re=2000$ to 5000. It is seen that with increasing Reynolds numbers both force coefficients are converging to a certain value. This could be seen in Figure 5.10 by comparing $Re=4000$ and $Re=5000$ cases for both forces. The lift and drag coefficient curves become smoother with increasing Reynolds number and also the amplitude of peaks and deeps of these curves increase. The difference between the upstroke and downstroke decreases with increasing Reynolds number and the effect of asymmetry starts to decrease.

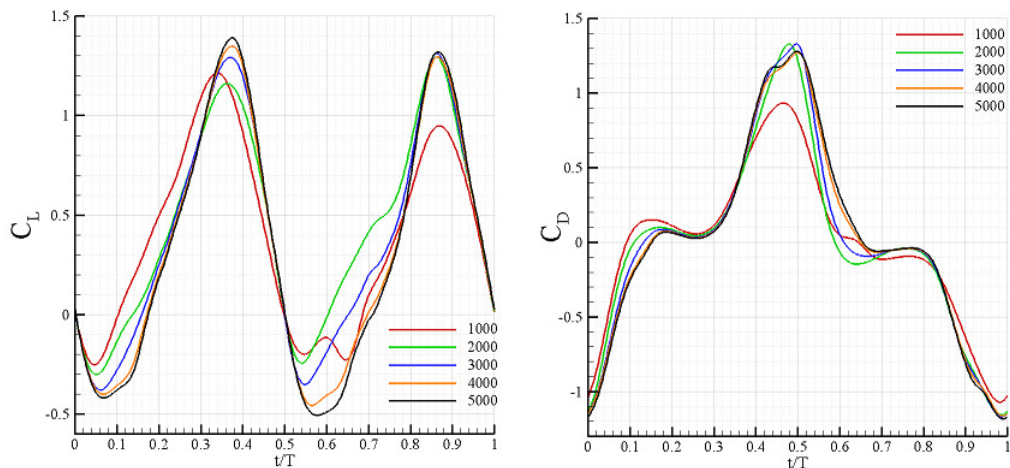


Figure 5.10 Time histories of lift and drag coefficients for $Y=0.5$ hovering at different Reynolds numbers.

There are differences in the lift coefficient histories at the beginning of the strokes for different Reynolds numbers. These differences occur due to the rotation of the airfoil. Since the airfoil is vertical at $t/T=0$, the lift coefficient is zero and the drag coefficient is in its minimum value over the period. The same situation also occurs at the beginning of the upstroke at $t/T=0.5$ but this time the drag coefficient is in its maximum value due to the definition of reference frame. To understand the effect of Reynolds number on instantaneous vortex field and the reason of the aforementioned differences in lift coefficient, the vorticity contours are investigated. Figure 5.10 shows the normalized vorticity contours starting from $t/T=0$ to $t/T=0.15$ at five different Reynolds numbers for which the lift coefficient histories are given in Figure 5.10. It is observed that the general vortex field does not differ significantly with Reynolds number. The former LEV is more diffusive at $Re=1000$ and it becomes stronger with increasing Reynolds number. This could also be seen in the lift coefficient history as a larger drop in lift. At all Reynolds numbers the airfoil moves without hitting the LEV, but with increasing Reynolds number, the vortex core becomes more closer to the airfoil surface. In Figure 5.10, between $t/T=0$ and $t/T=0.1$ there is a slight time delay between the deeps of lift coefficients at different Reynolds number due to the increasing strength of the vortices. Another effect could be different positions between the vortex core and the airfoil in Fig 5.11 for altering Reynolds numbers. The formation and detachment of LEV is more immediate with decreasing Reynolds number.

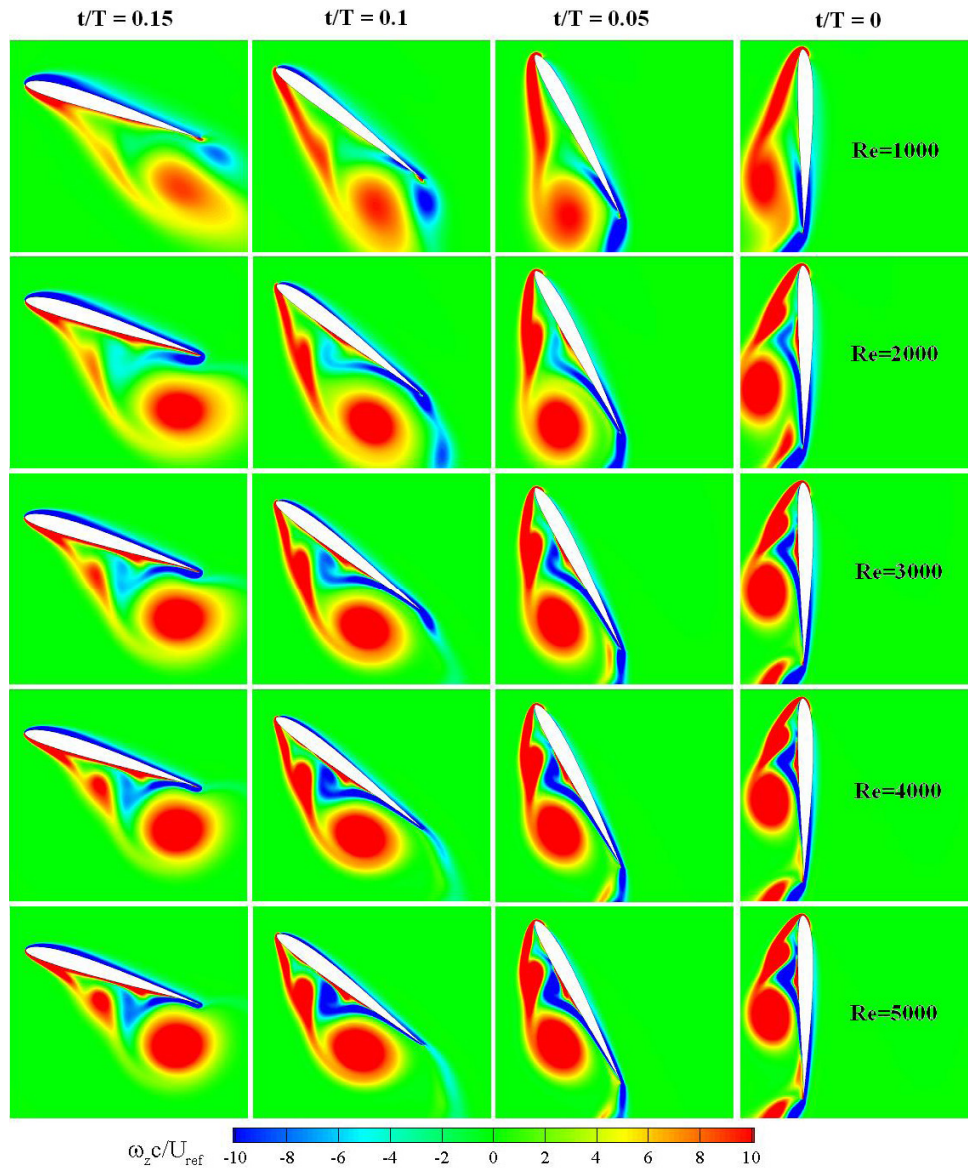


Figure 5.11 Instantaneous normalized vorticity contours for at the beginning of the period for different Reynolds numbers.

A clockwise rotation region is observed on the lower surface of the airfoil in Figure 5.11 at $t/T=0.0$. This clockwise rotation grows at all Reynolds numbers but become stronger with increasing Reynolds number. The clockwise rotation on the lower surface also decreases with time at all Reynolds numbers.

Figure 5.12 shows the mean drag and mean lift coefficient values for different Reynolds numbers. The convergence characteristic of hovering motion could also be

observed in Figure 5.12 for both force coefficients. The differences in mean lift and drag coefficients decrease for Reynolds numbers higher than 4000. There is a negligible difference in mean lift coefficients after $Re=4500$. The lift curve also reaches its peak value at $Re=2000$. This value seems to be the optimum value for hovering where the major aim is to have the maximum lift.

The mean drag coefficient curve does not seem to follow a general trend as in lift coefficient curve. For the maximum values of mean lift coefficients, the mean drag values are one order of magnitude smaller than their counterparts at $Re=500$ and 2500 . The smaller mean drag coefficient means that there will be fewer oscillations during the motion. Therefore most of the energy will be used for the main objective of lift generation. As in lift coefficient curve after $Re=4500$ also the mean drag coefficient values converge to a certain value of $\overline{C_D} = 0.025$.

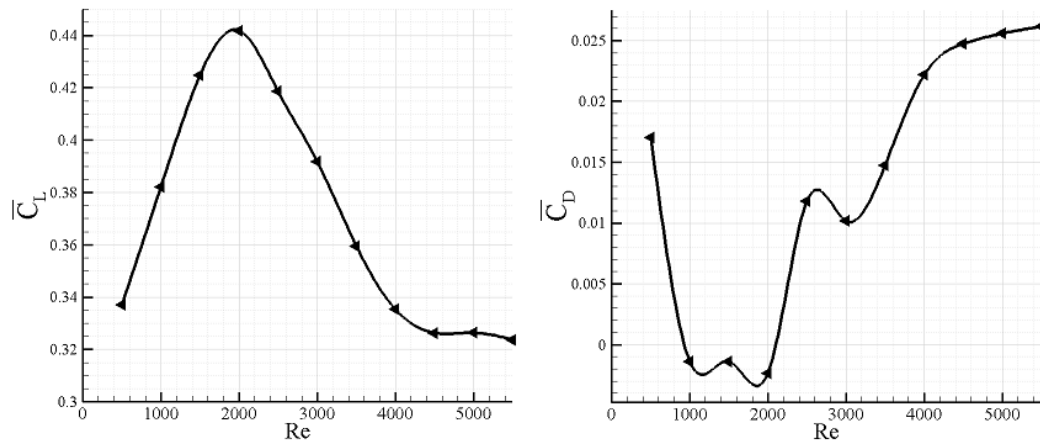


Figure 5.12 Mean lift (left) and drag (right) coefficients for $Y=0.5$ hovering at different Reynolds numbers.

Even there are slight differences in time histories of force coefficients, there are significant differences in mean values. The drag coefficient values are one order of magnitude smaller than the lift coefficient values so the drag curve is much more complex than the lift curve. As opposed to the forward flight, in hover, the important component of the force is the lift and it is observed that the lift follows a general trend with increasing Reynolds number. At last the $Y=0.5$ case at $Re=2000$ is found

as the most efficient case among the studied cases with greatest mean lift coefficient and the lowest mean drag coefficient. After that study it is observed that the lift coefficient is following a trend with altering Reynolds numbers. Thus, the most efficient Reynolds number regime for a certain figure-of-eight motion could be found out after a series of computations. This study just includes symmetric figure-of-eight motions but it could be expanded to asymmetric hovering motions to see that if the general trend, $\overline{C_L}$ vs Re, is related to the symmetry of the motion, or not.

CHAPTER VI

CONCLUDING REMARKS

The low Reynolds number aerodynamics of flapping motion is investigated numerically around an airfoil in forward flight and in hover. The flowfields around the airfoil are visualized via solving the Navier-Stokes equations with and without turbulence models depending on the Reynolds number. The force time histories, normalized velocity and vorticity contours are visualized for each mode of motion. The effects of reduced frequency, Reynolds number and airfoil geometry on unsteady aerodynamics of flapping airfoils are discussed.

The forward flapping flight cases include pitching and plunging of the airfoil in the existence of free stream velocity. The Reynolds-averaged Navier-Stokes equations coupled with Menter's Shear Stress turbulence model are solved on deforming O-type grids with Fluent 6.3. The hovering cases include vertical and horizontal translation coupled with pitching of the airfoil. For this case, Navier Stokes equations are solved on moving O-type grids with the same solver. For both flight modes the appropriate time-step and grid refinement studies are followed.

As a first study, the plunging and combined pitching and plunging of SD7003 airfoil are studied. For both motions LEV formations are observed. The pure plunging motion experiences a deep stall due to the more aggressive effective angle of attack history. It is found out that the numerical solutions agree well with experiments in deep dynamic stall rather than the more gentle pitching plunging motion that experiences light dynamic stall. It is concluded that the present numerical method

could predict the turbulent flowfield and instantaneous aerodynamic forces well and could be used as a design tool for MAV-based unsteady aerodynamic analyses.

The effect of airfoil geometry is studied with a flat plate that is performing the same motions at the same Reynolds number and reduced frequency. The flat plate case is a kind of fundamental case for which the geometry itself is not introducing a pressure gradient. It is observed that the LEV formation is more durable and stronger in flat plate case. The rounded edges are forcing the flat plate towards transition thus a deeper dynamic stall is observed.

The effect of reduced frequency on unsteady aerodynamics of a flapping airfoil in forward flight is also studied. In order to balance the Strouhal number, the plunging amplitude is decreased with increased reduced frequency. For both motions no large separations are observed. The wakes of the airfoils only produce Karman vortex streets. The instantaneous forces are found to follow the effective angle of attack history without effecting from the small vortices on the airfoil. It could be concluded that the Theodorsen's method is a suitable method for calculating the force coefficients at high reduced frequency, low plunging amplitude cases for which the method only includes the acceleration and circulatory effects. It is also observed that at high reduced frequencies the LEVS do not have sufficient time to grow.

The last study on the forward flapping flight is investigating the effect of Reynolds number. Both motions are studied for the Reynolds number values ranging from 10000 to 60000. It is found that general flow field and force time histories are not altering significantly for pure plunge motion for different Reynolds numbers. On the other hand, it is observed that there is a delay in LEV formation with decreasing Reynolds numbers. This delay also causes to decrease of the suction region on the airfoil in a shorter time. This is not a favorable situation for which this suction region is the main mechanism that is creating the lift enhancement during flapping.

The latter studies include the hovering flight of flapping wings. The effect of two similitude parameters, Reynolds number and reduced frequency, are investigated.

The reduced frequency is turned out to be only related with the vertical translation of the airfoil for figure of eight type hovering. Thus, a parametric study including seven different values of vertical translation and eleven different Reynolds numbers are performed.

In order to investigate the effect of reduced frequency on hovering aerodynamics seven different vertical translation amplitudes ranging from 0 to 1.5 are studied around SD7003 airfoil. For small values of vertical translation, LEV formations are observed at the end of the strokes whereas the LEV formations are shifted to the middle of the strokes with increasing amplitudes. With increasing amplitudes of vertical translation the separation becomes stronger but after a certain point the force coefficients tend to converge. For these values, in which the general flow field starts to converge, additional LEV formations are observed. The asymmetric airfoil also introduces differences between the upstroke and downstroke but this effect also decreases with increasing amplitudes of vertical translation. For the converged solutions, there is a negligible difference between the strokes due to the airfoil geometry. The acceleration effects dominate the flowfield and solution seems to be independent from the airfoil geometry. It is found that the $Y=0.5$ case is the optimum solution among the studied cases in terms of efficiency. Moreover, $Y=0.5$ case has a mean drag coefficient with one order of magnitude smaller than its counterparts.

The last study includes the investigation of Reynolds number effects on figure of eight hovering. The former most efficient case is studied at eleven different Reynolds numbers ranging from 500 to 5500 in the laminar regime. At all Reynolds numbers the flowfields found to be similar in terms of vorticity. Even no major difference is observed in terms of instantaneous force coefficient trends, the mean values are altering with Reynolds number. The mean aerodynamic force coefficients converge after $Re=4500$. It is meaningful to note that in hover the horizontal force component only introduces undesired oscillations which will consume energy. On the other hand, the vertical component is the only aim to keep the air vehicle in air during hover. Because of this, it is desired to have a Reynolds number regime in which the airfoil will have maximum mean lift and also the minimum mean drag coefficient. It

is found that the hovering airfoil has the maximum mean lift and minimum mean drag coefficient for the Reynolds number of 2000. It has been shown that there exists an efficient Reynolds number regime for figure of eight hovering. As a future work this trend could be investigated to see that if it is valid for all types of hovering motions or it is only valid for symmetric figure-of-eight motions.

REFERENCES

- [1] Ellington, C. P., *Insects versus birds: the great divide*, 44th AIAA Aerospace Sciences Meeting and Exhibit, Reno, Nevada, 9-12 January 2006.
- [2] Shyy, W., Lian, Y., Tang, J., Viieru, D., and Liu, H., *Aerodynamics of Low Reynolds Number Flyers*, Cambridge Univ. Press, New York, 2008.
- [3] McMichael, J. M., and Francis, M. S., *Micro Air Vehicles-Toward a New Dimension in Flight*, Defense Advanced Research Projects Agency, TTO Document, 1996.
- [4] Mueller, T. J., and DeLaurier, J.D., *An Overview of Micro Air Vehicle Aerodynamics*, in Mueller, T. J. (ed.), *Fixed and Flapping Wing Aerodynamics for Micro Air Vehicle Applications*, Vol. 195, Progress in Astronautics and Aeronautics, AIAA, Reston, VA, 2001.
- [5] Singh, B., and Chopra, I., *Insect-Based Hover-Capable Flapping Wings for Micro Air Vehicles: Experiments and Analysis*, AIAA Journal, Vol. 46, No. 9, pp. 2115-2135, 2008.
- [6] Mueller, T. J. (ed.), *Fixed and Flapping Wing Aerodynamics for Micro Air Vehicle Applications*, Vol. 195, Progress in Astronautics and Aeronautics, AIAA, Reston, VA, 2001.
- [7] Azuma, A., *The Biokinetics of Flying and Swimming*, 2nd ed., AIAA, Reston, VA, 2006.
- [8] Lehmann F. R., *Nature's Smart Engine: The Aerodynamics and Energetics of Flapping Insect Wings*, Imperial College Press, England, 2011.

- [9] Floreano, D., Zufferey, J-C., Srinivasan M. V., Ellington C., *Flying Insects and Robots*, Springer, New York, 2009
- [10] Kato, N., and Kamimura, S., *Bio-Mechanisms of Swimming and Flying: Fluid Dynamics, Biomimetic Robots, and Sports Science*, Springer-Verlag, New York, 2008.
- [11] Alexander, D.E. and Vogel, S., *Nature's Flyers: Birds, Insects, and the Biomechanics of Flight*, The Johns Hopkins University Press, Baltimore and London, 2002.
- [12] Henderson, C. L., and Adams, S., *Birds in Flight: The Art and Science of How Birds Fly*, 1st edition, Voyageur Press, 2008.
- [13] Vogel, S, *Life in Moving Fluids: the Philosophical Biology of Flow*, 2nd edition, Princeton University Press, New Jersey, 1996
- [14] Knoller, R., *Die Gesetze des Luftwiderstandes*, Flug- und Motortechnik (Wien), Vol.3, No. 21, pp. 1-7, 1909.
- [15] Betz, A., *Ein Beitrag zur Erlaerung des Segelfluges*, Zeitschrift fur Flugtechnik und Motorluftschiffahrt, Vol. 3, pp. 269-272, 1912.
- [16] Jones, K. D., Dohring, C. M., and Platzer, M. F., *Experimental and Computational Investigation of the Knoller-Betz Effect*, AIAA Journal, Vol. 36, No. 7, pp. 1240–1246, 1998.
- [17] Katzmayer, R., *Effect of Periodic Changes of Angle of Attack on Behavior of Airfoils*, NACA TM147, October 1922.
- [18] Platzer M.F., Jones, K. D., Young, J., and Lai, J., C., S., *Flapping-Wing Aerodynamics: Progress and Challenges*, AIAA Journal Vol. 46, No. 9, 2008.
- [19] Birnbaum, W. *Das ebene Problem des Schlagenden Fluegels*, Zeitschrift fuer Angewandte Mathematik und Mechanik, Vol. 4, No. 4, pp. 277-292, 1924.

- [20] von Karman, T., and Burgers, J. M., *General Aerodynamic Theory - Perfect Fluids*, Aerodynamic Theory, edited by W. F. Durand, Vol. 2, Julius Springer, Berlin, p.308, 1934
- [21] Theodorsen, T., *General Theory of Aerodynamic Instability and the Mechanism of Flutter*, NACA Report 496, 1935.
- [22] Babinsky, H., Baik Y., Bansmer S., Beran P., Bernal L., Günaydinoğlu, E., Kang C. K., Konrath R., Kurtuluş D. F., Ol M., Paquet J.B., Radespiel R., Reichert T., Rival D., Shyy W., Ukeiley L., Visbal M. R. and Yuan W., *Unsteady Aerodynamics for Micro Air Vehicles*, NATO-RTO, TR. AVT-149, 2010
- [23] Pesavento, U., and Wang Z. J, Theodorsen, T., *Flapping Wing Flight Can Save Aerodynamic Power Compared to Steady Flight*, Physical Review Letters, Vol. 103, 118102, 2009
- [24] McCroskey, W. J., Carr, L. W., and McAlister, K. W., *Dynamic Stall Experiments on Oscillating Airfoils*, AIAA J., Vol. 14, No. 1., pp. 57-63, 1976
- [25] Liiva, J., *Unsteady Aerodynamic and Stall Effects on Helicopter Rotor Blade Airfoil Sections*, J. Aircraft, Vol. 6, No.1, pp. 46-51, 1969.
- [26] McCroskey, W. J., *Unsteady Airfoils*, Annual Reviews of Fluid Mechanics, Vol. 14, pp. 285-311, 1982
- [27] Carr, L., *Progress in Analysis and Prediction of Dynamic Stall*, Journal of Aircraft, Vol. 25, pp. 6-17, 1988
- [28] Carr, L., and McCroskey, W. J., *A Review of Recent Advances in Computational and Experimental Analysis of Dynamic Stall*, IUTAM Symposium on Fluid Dynamics of High Angle of Attack, 1992
- [29] Ol, M. V., Eldredge, J. D., and Wang, C., *High-Amplitude Pitch of a Flat Plate: an Abstraction of Perching and Flapping*, International Journal of Micro Air Vehicles, Vol. 1, No. 3, pp. 203-216, 2009

- [30] Ol, M. V., Altman, A., Eldredge, J. D., Garmann, D. J, and Lian, Y., *Resume of the AIAA FDTC Low Reynolds Number Discussion Group's Canonical Cases*, AIAA-2010-1085, January 2010
- [31] I.H. Tuncer and M. Kaya, *Thrust Generation Caused by Flapping Airfoils in a Biplane Configuration*, Journal of Aircraft, Vol. 40, No.3, pp. 509-515, 2003
- [32] Kaya, M., Tuncer, I.H., Jones, K. D., and Platzer, M. F., *Optimization of Flapping Motion Parameters for Two Airfoils in a Biplane Configuration*, Journal of Aircraft, Vol. 46, No. 2, 2009
- [33] Taylor, G. K., Nudds, R. L., and Thomas, A. L. R., *Flying and Swimming Animals Cruise at a Strouhal Number Tuned for High Power Efficiency*, Nature (London), Vol. 425, pp. 707–711, 2003.
- [34] Tuncer, I.H. and Kaya, M., *Optimization of Flapping Airfoils For Maximum Thrust and Propulsive Efficiency*, AIAA Journal, Vol 43, p: 2329-2341, 2005.
- [35] Günaydınoğlu, E., and Kurtuluş, D.F., *Numerical Investigation of Pure Plunge and Pitch/Plunge Motions at Low Reynolds Numbers*, International Symposium of Light-Weight Unmanned Aerial Vehicle Systems and Subsystems, Ostend, Belgium, 11-13 March 2009
- [36] Günaydınoğlu, E., and Kurtuluş, D.F., *Flow Characteristics of Pitching and Plunging SD7003 Airfoil for Different Reduced Frequencies*, Ankara International Aerospace Conference, Ankara, Turkey, 17-19 August 2009
- [37] Günaydınoğlu, E., and Kurtuluş, D.F., *Unsteady Aerodynamic Analysis of a Flapping Flat Plate at Low Reynolds Numbers*, First International Workshop on Computational Engineering - Special Topic Fluid-Structure Interaction. Research Unit 493 Fluid-Structure Interaction: Modelling, Simulation, Optimisation, Herrsching, Germany, 12-14 October 2009
- [38] Günaydınoğlu, E., and Kurtuluş, D.F., *Çırpan Düz Levha Kesiti Etrafındaki Akışın Sayısal Yöntemlerle İncelenmesi*, 5. Savunma Teknolojileri kongresi SAVTEK 2010, Orta Doğu Teknik Üniversitesi, Ankara, 23-25 Haziran 2010

- [39] McMasters, J. H., and Henderson, M. J., *Low speed single elementairfoil synthesis*, Technical Soaring, Vol. 6, pp. 1-21, 1980
- [40] Freymuth, P., *Thrust generation by an airfoil in hover modes*, Experiments in Fluids, Vol. 9, pp. 17-24, 1990.
- [41] Wang, Z. J., *Vortex Shedding and Frequency Selection in Flapping Flight*, Journal of Fluid Mechanics, Vol. 410, pp. 323-341, 2000.
- [42] Hall, K. C., Pigott, S. A., and Hall, S. R., *Power Requirements for Large-Amplitude Flapping Flight*, Journal of Aircraft, Vol. 35, No. 3, pp. 352-361, 1998
- [43] Wang, Z. J., *Two Dimensional Mechanism for Insect Hovering*, Physical Review Letters, Vol. 85, No. 10, September 2000.
- [44] Rayner, J. M. V., *A vortex theory of animal flight. Part 1. The vortex wake of a hovering animal*, Journal of Fluid Mechanics, Vol. 91, pp. 697-730, 1979
- [45] Lighthill, M., *Mathematical biofluidynamics*, In Regional Conference Series in Applied Mathematics, vol. 17, Philadelphia: Society for Industrial and Applied Mathematics, 1975
- [46] Berman, G.J. and Wang, Z.J., *Energy-minimizing kinematics in hovering insect flight*, Journal of Fluid Mechanics, Vol. 582, pp.153-167, 2007
- [47] Lehmann, F.-O. and Pick, S., *The aerodynamic benefit of wing–wing interaction depends on stroke trajectory in flapping insect wings*, The Journal of Experimental Biology, Vol. 210, pp.1362-1377, 2007
- [48] Dickinson, M. H., Lehmann F.-O., and Sane, S. P., *Wing Rotation and the Aerodynamic Basis of Insect Flight*, Science, Vol. 284, pp.1954-1960, 1999
- [49] Wang, Z. J. and Russell, D., *Effect of Forewing and Hindwing Interactions on Aerodynamic Forces and Power in Hovering Dragonfly Flight*, Phys. Rev. Lett., Vol. 99, 148101, 2007

- [50] Maxworthy, T., *The Fluid Dynamics of Insect Flight*, Ann. Rev. Fluid. Mech., Vol. 198, No. 13, 1981.
- [51] Ellington, C. P., Van den Berg, C., Willmott, A. P. and Thomas, A. L. R., *Leading-edge vortices in insect flight*, Nature, Vol. 384, pp. 626-630, 1996
- [52] Van den Berg, C., Ellington, C. P., *The three-dimensional leading-edge vortex of a 'hovering' model hawkmoth*, Phil. Trans. R. Soc. Lond. B, Vol. 352, pp. 329-340, 1997.
- [53] Günaydınoğlu, E., and Kurtuluş, D.F., *Effect of Vertical Translation on Unsteady Aerodynamics of a Hovering Airfoil*, Fifth European Conference on Computational Fluid Dynamics ECCOMAS CFD 2010, Lisbon, Portugal, 14-17 June 2010
- [54] Günaydınoğlu, E., and Kurtuluş, D.F., *Reynolds Sayısının Havada Asılı Sekiz Hareketi Yapan Kanat Kesiti Aerodinamiğine Etkisi*, III. Ulusal Havacılık ve Uzay Konferansı, Eskişehir, Türkiye, 16-18 Eylül 2010
- [55] *Fluent v.6.3 User's Guide*, 2006.
- [56] Menter, F. R., Menter, F.R., *Two-Equation Eddy-Viscosity Turbulence Models for Engineering Applications*, AIAA Journal, Vol. 32, No. 8, pp. 1598-1605, August 1994
- [57] Ekaterinaris J. A., Menter F.R., *Computation of Oscillating Airfoil Flows with One- and Two-Equation Turbulence Models*, AIAA Journal, Vol. 32, No. 12, pp. 2359-2365, December 1994
- [58] Patankar, S. V., *Numerical Heat Transfer and Fluid Flow*, Hemisphere Publishing Corporation, Washington New York London, 1980.
- [59] Ol, M.V., Bernal, L., Kang, C.K., Shyy, Wei., *Shallow and Deep Dynamic Stall for Flapping Low Reynolds Number Airfoils*, Experiments in Fluids, Vol. 46, 883-901, April 2009

- [60] Yuan, W., and Khalid, M., *Flow Analysis of a Flapping SD7003 Airfoil at Transitional Reynolds Numbers*, 27th AIAA Applied Aerodynamics Conference, San Antonio, Texas, AIAA 2009-3955, June 2009
- [61] OL, M. V., *Vortical Structures in High Frequency Pitch and Plunge at Low Reynolds Number*, 37th AIAA Fluid Dynamics Conference and Exhibit, 25 - 28 June 2007, Miami, FL, AIAA 2007-423, 2007.
- [62] Başkan, Ö., *Experimental and Numerical Investigation of Flow Field Around Flapping Airfoil Making Figure-of-Eight in Hover*, M.Sc. Dissertation, METU Aerospace Engineering Department, September 2009.
- [63] Jardin, T., David L., and Farcy, A., *Characterization of vortical structures and loads based on time-resolved PIV for asymmetric hovering flapping flight*, Experiments in Fluids, Vol. 46, No.5, pp. 847-857, 2009